Giant optical activity and Kerr effect in type-I and type-II Weyl semimetals

Kabyashree Sonowal,[1] Ashutosh Singh,[1,2] and Amit Agarwal[1,*]
[1]*Department of Physics, Indian Institute of Technology Kanpur, Kanpur 208016, India*
[2]*Department of Physics and Astronomy, McMaster University, Hamilton, Ontario L8S 4M1, Canada*

(Received 26 March 2019; published 28 August 2019)

We explore optical activity in thin films and bulk of type-I and type-II Weyl semimetals (WSMs), and demonstrate the existence of a giant Kerr effect in both. In time reversal symmetry broken WSM thin films, the polarization rotation is caused by the optical Hall conductivity including the anomalous Hall term. The Kerr angle is found to be $\propto Q/\omega$, with Q and ω being the Weyl node separation and the optical frequency, respectively. In contrast, the optical activity in the bulk WSM is dominated by axion electrodynamics, which persists even in the Pauli-blocked regime of no optical transitions. In bulk WSMs, Q acts analogously to the magnetization in magnetic materials, leading to a large polar Kerr effect (linear in Q), when light is incident on the WSM surface without Fermi arc states, and the Voigt effect (quadratic in Q), when light is incident on surface with Fermi arc states.

DOI: 10.1103/PhysRevB.100.085436

I. INTRODUCTION

Weyl semimetals host even pairs of linearly dispersing massless quasiparticles of opposite chirality with novel Fermi arc surface states [1–7]. Their existence has been recently demonstrated in several crystalline materials with broken time-reversal or space-inversion symmetry. Some examples include topological insulator material [8], pyrochlore iridates [2,9], WTe_2 [10,11], $MoTe_2$ [12–17], $Mo_xW_{1-x}Te_2$ [18,19], TaAs [20–23], and TaP [24–26], among others. In contrast to their high-energy counterparts, Weyl semimetals (WSMs) can also have a Lorentz symmetry violating tilted energy spectrum. This allows their classification into a type-I (partially tilted) WSM with vanishing density of states (DOS) at the Weyl point, and a type-II (overtilted) phase with a finite DOS at the Fermi energy and an electron and a hole pocket on either side of the Weyl point [3]. The type-II Weyl state has been experimentally demonstrated in noncentrosymmetric $TaIrTe_4$ [27], $MoTe_2$ [13], WTe_2 [17], and LaAlGe [28], among other materials.

The Weyl nodes in a WSM act as a source or sink of the Berry curvature, which acts as a magnetic field in the momentum space [29–32]. This finite Berry phase induces several very interesting electronic transport and optical phenomena, including the quantum anomalous Hall (QAH) effect [29,32–53]. Another intriguing aspect of optical activity in WSMs is its connection to axion electrodynamics [54,55], which modifies the Maxwell equations. The combined effect of these has led to the prediction of several interesting effects in WSMs interacting with light, such as giant polarization rotation [47], tunable perfect absorption [50], and creation of novel waveguide modes [51]. Contact-free optical techniques such as polarization rotation are also regularly used to explore time reversal symmetry breaking states in ferromagnets [56], multiferroics [57], superconductors [58], and the QAH state in graphene [59] and topological insulators [60].

Here, we demonstrate the existence of giant polarization rotation in the electrodynamic response in tilted WSMs with broken time-reversal symmetry. Our results generalize the study of Ref. [47] to include the impact of the tilt in type-I and type-II WSMs and a finite chemical potential. To this end, we analytically calculate the full complex optical conductivity matrix for tilted type-I and type-II WSMs including finite chemical potential and the internodal separation. This allows us to obtain the exact polarization rotation for the thin-film geometry as well as for bulk WSMs, without using any small-angle approximation.

In WSM thin films, the giant Kerr rotation (GKR), polarization rotation in the reflected beam, originates from the optical Hall conductivity including the QAH effect. We analytically calculate the full optical conductivity matrix $\sigma_{ij}(\omega)$ for tilted type-I and type-II WSMs and find that all the diagonal components $\sigma_{ii} \propto \omega$, while the off-diagonal Hall term $\sigma_{xy} \propto Q$, where Q denotes the Weyl node separation (in the z direction) and $\sigma_{xz} = \sigma_{yz} = 0$. For light incident on the WSM thin film surface without the Fermi arc states (perpendicular to the node separation), the Kerr angle $\Theta_{\rm Kerr} \propto \sigma_{xy}/\sigma_{xx} \propto Q/\omega$. For realistic material parameters, the Kerr angle is found to be of the order of 10^{-1} radians for optical frequencies below 10^{14} Hz. This is "giant" compared to the usually observed values of 10^{-6} to 10^{-4} radians in topological insulators and magnetic and other materials [47,56,58,59]. For light incident on the surface with Fermi arc states (parallel to the node separation), we find that $\Theta_{\rm Kerr} \propto \sigma_{yz}/\sigma_{zz} = 0$.

In bulk WSM large optical activity is predominantly caused by the axion electrodynamics induced changes in the Maxwell equations. The effective dielectric constant of the modified Maxwell equation can be expressed as $\epsilon'_{ij} = \epsilon_{ij} + \varepsilon_{ijk}Q_k \times 2i\alpha_F c/(\pi\omega)$, where the second term establishes Q/ω to be the effective "gyrotropy" constant, analogous to magnetization in magnetic systems. This axion-induced gyrotropy is what leads

*amitag@iitk.ac.in

to optical activity in bulk WSMs, even in the Pauli-blocked regime with forbidden optical transitions. For light incident parallel to the Weyl node separation (on surfaces without Fermi arc states), only circular eigenmodes are allowed in the WSM, leading to large circular birefringence and circular dichroism, along with the giant Kerr effect, which is odd in Q. For light incident on surface perpendicular to the Weyl node separation (on surfaces with Fermi arc states), there is large linear birefringence and dichroism, along with a polarization angle dependent giant Kerr effect which is an even function of Q.

This paper is organized as follows: In Sec. II we discuss the formalism for calculating optical conductivity for a generic two-band model, based on the optical Bloch equation. In Sec. III, we obtain the optical conductivity matrix for tilted type-I and type-II WSMs, including the QAH contribution. In Sec. IV we discuss the electromagnetic response in thin films of tilted WSM, and demonstrate the existence of giant polarization rotation. This is followed by a discussion of axion electrodynamics induced large optical activity in bulk WSMs in Sec. V. Finally, we summarize our findings in Sec. VI.

II. LIGHT-MATTER INTERACTION IN WSMs

The low-energy properties of a generic two-band system can be described using the following 2×2 Hamiltonian,

$$\hat{H}_0 = \sum_{\boldsymbol{k}} \mathbf{h}_{\boldsymbol{k}} \cdot \boldsymbol{\sigma}. \tag{1}$$

Here, $\mathbf{h}_{\boldsymbol{k}} = (h_{0\boldsymbol{k}}, h_{1\boldsymbol{k}}, h_{2\boldsymbol{k}}, h_{3\boldsymbol{k}})$ is a vector composed of real scalar functions of $\boldsymbol{k}$, and $\boldsymbol{\sigma} = (\mathbb{1}_2, \sigma_x, \sigma_y, \sigma_z)$ is a vector composed of the identity and the three 2×2 Pauli matrices. The interaction with an electromagnetic field is modeled using the dipole approximation, $\hat{H} = \hat{H}_0 + e\mathbf{E} \cdot \hat{\mathbf{r}}$. Here e is the electronic charge, and $\mathbf{E}$ is the electric field.

Now, physical observables can be calculated using the optical Bloch equation for the dynamics of the density matrix [61,62]. The corresponding interband contribution to the current (for a given $\boldsymbol{k}$) in the *linear response regime* is given by

$$\mathbf{J}_{\mathbf{k}}(\omega) = -\frac{i n_{\boldsymbol{k}}^{\mathrm{eq}}}{\hbar\omega_{\boldsymbol{k}}} \left[\frac{(\mathbf{E} \cdot \mathbf{M}_{\boldsymbol{k}}^{vc})\mathbf{M}_{\boldsymbol{k}}^{cv}}{\omega + \omega_{\boldsymbol{k}} + i\gamma} + \frac{(\mathbf{E} \cdot \mathbf{M}_{\boldsymbol{k}}^{cv})\mathbf{M}_{\boldsymbol{k}}^{vc}}{\omega - \omega_{\boldsymbol{k}} + i\gamma} \right]. \tag{2}$$

Here, $n_{\boldsymbol{k}}^{\mathrm{eq}} = f(\epsilon_{\mathbf{k}}^{c}, \mu) - f(\epsilon_{\mathbf{k}}^{v}, \mu)$ is the equilibrium population difference between the conduction and the valance band and $\mathbf{M}_{\boldsymbol{k}}^{vc} \equiv \langle \psi_{\boldsymbol{k}}^{v} | e\nabla_{\boldsymbol{k}} \hat{H}_0/\hbar | \psi_{\boldsymbol{k}}^{c} \rangle = (\mathbf{M}_{\boldsymbol{k}}^{cv})^*$ is the optical matrix element responsible for vertical transition between valence and conduction band. The transition energy is denoted by $\hbar\omega_{\boldsymbol{k}} = \varepsilon_{\boldsymbol{k}}^{c} - \varepsilon_{\boldsymbol{k}}^{v}$ and γ is the phenomenological damping term for the interband coherence (off-diagonal elements of the density matrix). The interband optical conductivity obtained from Eq. (2) in the limiting case of $\gamma \to 0$ is equivalent to the Kubo formula for a two-band system. It is given by

$$\sigma_{\alpha\beta}(\omega) = -\lim_{\gamma\to 0} \sum_{\boldsymbol{k}} \frac{i n_{\boldsymbol{k}}^{\mathrm{eq}}}{\hbar\omega_{\boldsymbol{k}}} \times \left[\frac{(\mathbf{M}_{\boldsymbol{k}}^{vc} \otimes \mathbf{M}_{\boldsymbol{k}}^{cv})_{\alpha\beta}}{\omega + \omega_{\boldsymbol{k}} + i\gamma} + \frac{(\mathbf{M}_{\boldsymbol{k}}^{cv} \otimes \mathbf{M}_{\boldsymbol{k}}^{vc})_{\alpha\beta}}{\omega - \omega_{\boldsymbol{k}} + i\gamma} \right] \tag{3}$$

with $\otimes$ denoting the outer product of the optical matrix element vectors.

Now let us consider a simple continuum model of a WSM with a pair of oppositely tilted Weyl nodes, with chirality $\xi = \pm 1$ located in the Brillouin zone at $\boldsymbol{k} = \{0, 0, \mp Q\}$. The low-energy Hamiltonian of a Weyl node [63–66] of chirality ξ can be expressed in the form of Eq. (1), with the following mapping: $h_{0\mathbf{k}} = \hbar\xi v_t k_z^{\xi}$, $h_{1\mathbf{k}} = \xi\hbar v_F k_x$, $h_{2\mathbf{k}} = \xi\hbar v_F k_y$, and $h_{3\mathbf{k}} = \xi\hbar v_F k_z^{\xi}$, to yield

$$\hat{H}_{\xi} = \hbar\xi v_t k_z^{\xi} \mathbb{1} + \xi\hbar v_F \left[k_x\sigma_x + k_y\sigma_y + k_z^{\xi}\sigma_z \right], \tag{4}$$

where $k_z^{\xi} = k_z + \xi Q$. Here, v_t is the tilt velocity of the $\xi = +1$ Weyl node and v_F is the Fermi velocity. The degree of tilt of the Weyl nodes is characterized by $\alpha_t = v_t/v_F$, with $|\alpha_t| < 1$ being a type-I Weyl node, and $|\alpha_t| > 1$ being a type-II Weyl node. Eigenvalues of Eq. (4) are given by $\varepsilon_{\boldsymbol{k}}^{\lambda} = \hbar\xi v_t k_z^{\xi} + \lambda\hbar v_F k_{\xi}$, where $\lambda = 1$ (-1) denotes the conduction (valance) band. Here, we have defined $k_{\xi} = [k_x^2 + k_y^2 + (k_z^{\xi})^2]^{1/2}$.

The dimensionless optical matrix element corresponding to Eq. (4) is given by $\tilde{\mathbf{M}}_{\boldsymbol{k}}^{vc} \equiv \mathbf{M}_{\boldsymbol{k}}^{vc}/ev_F$

$$= \left(i\sin\phi_{\boldsymbol{k}} - \xi\tilde{k}_z\cos\phi_{\boldsymbol{k}}, -i\cos\phi_{\boldsymbol{k}} - \xi\tilde{k}_z\sin\phi_{\boldsymbol{k}}, \xi\frac{k_{\perp}}{k_{\xi}} \right). \tag{5}$$

Here, we have defined $\tilde{k}_z = k_z^{\xi}/k_{\xi}$, $\phi_{\boldsymbol{k}} = \tan^{-1}(k_y/k_x)$, and $k_{\perp} = (k_x^2 + k_y^2)^{1/2}$. Note that $\tilde{\mathbf{M}}_{\boldsymbol{k}}^{vc}$ does not depend on the tilt velocity v_t at all.

We now calculate the optical conductivity matrix of the tilted type-I and type-II WSMs, in the next section. These will be used to calculate the polarization rotation (Kerr angle and ellipticity) of a linearly polarized optical beam reflected from WSM thin films, and from bulk WSMs. In both cases, the polarization rotation (Φ) and the ellipticity angle (Ψ) can be expressed in terms of a complex dimensionless quantity (χ) via the relation [67]

$$\tan(2\Phi) = \frac{2\mathrm{Re}[\chi]}{1 - |\chi|^2} \quad \text{and} \quad \sin(2\Psi) = \frac{2\mathrm{Im}[\chi]}{1 + |\chi|^2}. \tag{6}$$

In the limiting case of $|\chi| \ll 1$, Eq. (6) can be simplified as $\Phi \approx \mathrm{Re}[\chi]$ and $\Psi \approx \mathrm{Im}[\chi]$. However, unlike the case of magnetic materials [68] where $|\chi| \ll 1$, for the case of WSMs we find that in general $|\chi| \sim 1$, and the exact Eq. (6) has to be used.

III. OPTICAL CONDUCTIVITY MATRIX OF TYPE-I AND TYPE-II WSMs

Calculating the optical conductivity of the tilted type-I and type-II WSMs described by Eq. (4), we find that $\sigma_{xx} = \sigma_{yy}$, $\sigma_{xy} = -\sigma_{yx}$, and the remaining off-diagonal elements of the conductivity matrix are zero, $\sigma_{xz} = \sigma_{yz} = \sigma_{zx} = \sigma_{zy} = 0$. The vertical transitions responsible for the optical conductivities of type-I and type-II WSMs are shown in Figs. 1(a) and 1(b), respectively. For simplicity, we will work in the zero-temperature regime where the Fermi function can be replaced by the corresponding Heaviside step function.

A. $\sigma_{xx}(\omega)$

The real part of the longitudinal conductivity σ_{xx} has been calculated in Ref. [69], and our calculations (detailed in

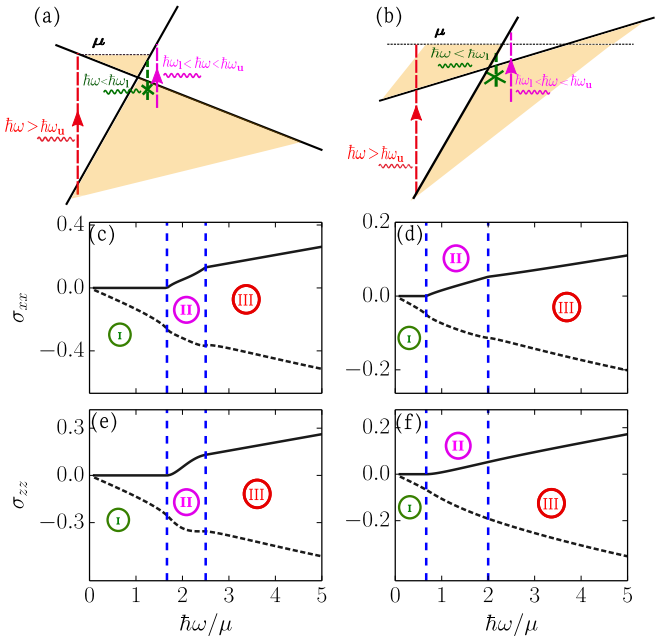

FIG. 1. (a), (b) Schematic of the Pauli-blocking and allowed vertical optical transitions in a type-I and a type-II WSM, respectively. The region of $\omega < \omega_l$ (region I) is completely Pauli blocked for vertical transitions while the region II, $\omega_l < \omega < \omega_u$, is partially Pauli blocked, and in region III, $\omega > \omega_u$, the full phase space is available for vertical transitions. (c), (d) show the real (solid line) and the imaginary part (dashed line) of the σ_{xx}, in a type-I ($\alpha_t = 0.2$) and a type-II ($\alpha_t = 2.0$) WSM, respectively. (e), (f) show the real (solid line) and the imaginary part (dashed line) of σ_{zz}, in a type-I ($\alpha_t = 0.2$) and a type-II ($\alpha_t = 2.0$) WSM, respectively. The vertical lines mark the boundary values of transition energy, $\hbar\omega_l = 2\mu/(1 + |\alpha_t|)$ (green), and $\hbar\omega_u = 2\mu/(1 - |\alpha_t|)$ (red) or $\hbar\omega'_u = 2\mu/(|\alpha_t| - 1)$ (red) in a type-II WSM. Here, the conductivities are scaled in units of $\sigma_Q = e^2Q/(\pi h)$, and we have chosen $\mu/(\hbar v_F Q) = 0.1$.

Appendix A) based on Eq. (3) reproduce those results. To start with, we calculate the real and imaginary part separately by using the Dirac identity on Eq. (3). For a type-I WSM hosting a pair of oppositely tilted Weyl nodes with $|\alpha_t| < 1$, we obtain

$$\mathrm{Re}[\sigma_{xx}(\omega)] = \begin{cases} 0, & \mathrm{I}: \ \omega < \omega_l, \\ \sigma_\omega(1/2 - \eta_1), & \mathrm{II}: \ \omega_l < \omega < \omega_u, \\ \sigma_\omega, & \mathrm{III}: \ \omega > \omega_u. \end{cases} \tag{7}$$

Here we have defined a conductivity scale set by the optical frequency: $\sigma_\omega = e^2\omega/(6hv_F)$. The photon energy bounds are $\hbar\omega_l = 2\mu/(1 + |\alpha_t|)$, $\hbar\omega_u = 2\mu/(1 - |\alpha_t|)$, and

$$\eta_1 = \frac{3}{8|\alpha_t|}\left(\frac{2\mu}{\hbar\omega} - 1\right)\left[1 + \frac{1}{3\alpha_t^2}\left(\frac{2\mu}{\hbar\omega} - 1\right)^2\right]. \tag{8}$$

Basically, in region I for $\omega < \omega_l$, the phase space for vertical transitions is Pauli blocked, as shown in Fig. 1. For region II, $\omega \in (\omega_l, \omega_u)$, the Pauli blocking gets removed with increasing energy resulting in finite vertical transitions and finite $\mathrm{Re}[\sigma_{xx}(\omega)]$. In the $\alpha_t \to 0$ limit we have $\omega_l \to \omega_u = 2\mu/\hbar$, and we have $\mathrm{Re}[\sigma_{xx}(\omega)] = \sigma_\omega$ for $\hbar\omega \geqslant 2\mu$. In the other limit $\alpha_t \to 1$, we have $\omega_u \to \infty$ with region II extending to higher energies.

For the type-II Weyl node with $|\alpha_t| > 1$, we obtain

$$\mathrm{Re}[\sigma_{xx}(\omega)] = \begin{cases} 0, & \mathrm{I}: \ \omega < \omega_l, \\ \sigma_\omega(1/2 - \eta_1), & \mathrm{II}: \ \omega_l < \omega < \omega'_u, \\ \sigma_\omega\eta_2, & \mathrm{III}: \ \omega > \omega'_u. \end{cases} \tag{9}$$

Here we have defined $\hbar\omega'_u = 2\mu/(|\alpha_t| - 1)$, and

$$\eta_2 = \frac{3}{4|\alpha_t|}\left[1 + \frac{1}{3\alpha_t^2} + \left(\frac{2\mu}{\alpha_t\hbar\omega}\right)^2\right]. \tag{10}$$

The imaginary part of the longitudinal optical conductivity $\sigma_{xx}(\omega)$, for a type-I WSM, for $|\alpha_t| < 1$ is calculated to be

$$\frac{\mathrm{Im}[\sigma_{xx}]}{\sigma_\omega} = \frac{-1}{4\pi}\left\{\tau(\alpha_t)\ln\left[\frac{|\omega_u^2 - \omega^2|}{|\omega_l^2 - \omega^2|}\right] + \frac{8}{\alpha_t^2}\left(\frac{\mu}{\hbar\omega}\right)^2 - \left(\frac{\mu}{\hbar\omega}\right)^3\Pi(\omega, \alpha_t, \mu)\ln\left[\frac{|\omega_u - \omega|(\omega_l + \omega)}{|\omega_l - \omega|(\omega_u + \omega)}\right] + \frac{6}{|\alpha_t|^3}\left(\frac{\mu}{\hbar\omega}\right)^2\ln\left[\frac{|\omega_u^2 - \omega^2|\omega_l^2|}{|\omega_l^2 - \omega^2|\omega_u^2|}\right] + 4\ln\left[\frac{|\omega_c^2 - \omega^2|}{|\omega_u^2 - \omega^2|}\right]\right\}. \tag{11}$$

Here $\omega_c \equiv v_F k_c$ is the ultraviolet cutoff frequency (see Appendix A for details). For a type-II WSM, with $|\alpha_t| > 1$, we obtain

$$\frac{\mathrm{Im}[\sigma_{xx}]}{\sigma_\omega} = \frac{-1}{4\pi}\left\{\tau(\alpha_t)\ln\left[\frac{|\omega_u'^2 - \omega^2|}{|\omega_l^2 - \omega^2|}\right] + \frac{8}{\alpha_t^3}\left(\frac{\mu}{\hbar\omega}\right)^2 - \left(\frac{\mu}{\hbar\omega}\right)^3\Pi(\omega, \alpha_t, \mu)\ln\left[\frac{|\omega'_u - \omega|(\omega_l + \omega)}{|\omega_l - \omega|(\omega'_u + \omega)}\right] + \frac{6}{|\alpha_t|^3}\left(\frac{\mu}{\hbar\omega}\right)^2\ln\left[\frac{|\omega_u'^2 - \omega^2|\omega_l^2|}{|\omega_l^2 - \omega^2|\omega_u'^2|}\right] + \left(\frac{3}{|\alpha_t|} + \frac{1}{|\alpha_t|^3}\right)\ln\left[\frac{|\omega_c^2 - \omega^2|}{|\omega_u'^2 - \omega^2|}\right] + \frac{12}{|\alpha_t|^3}\left(\frac{\mu}{\hbar\omega}\right)^2\ln\left[\frac{|\omega_c^2 - \omega^2|\omega_u'^2|}{|\omega_u'^2 - \omega^2|\omega_c^2|}\right]\right\}. \tag{12}$$

In Eqs. (11) and (12), we have defined the following functions:

$$\tau(\alpha_t) = \frac{1}{2}\left(4 + \frac{1}{|\alpha_t|^3} + \frac{3}{|\alpha_t|}\right), \tag{13}$$

$$\Pi(\mu, \omega, \alpha_t) = \frac{4}{|\alpha_t|^3} + 3\left(\frac{\hbar\omega}{\mu}\right)^2\left(\frac{1}{|\alpha_t|^3} + \frac{1}{|\alpha_t|}\right). \tag{14}$$

In the limiting case of $\alpha_t \to 0$, Eq. (11) reduces to

$$\mathrm{Im}[\sigma_{xx}(\omega)] = -\frac{\sigma_\omega}{\pi} \ln \left| \frac{\omega_c^2 - \omega^2}{\omega^2 - 4(\mu/\hbar)^2} \right|. \tag{15}$$

In the intrinsic limit of $\mu \to 0$, we obtain

$$\lim_{\mu\to 0} \mathrm{Im}[\sigma_{xx}(\omega)] = \frac{-\sigma_\omega}{\pi} \ln \left| \frac{\omega_c^2 - \omega^2}{\omega^2} \right| \begin{cases} 1, & \text{type I,} \\ \frac{1+3\alpha_t^2}{2\alpha_t^3}, & \text{type II.} \end{cases} \tag{16}$$

Of these, the type-I result is independent of the tilt, and has been derived earlier in Refs. [47,49].

The real and the imaginary parts of $\sigma_{xx}(\omega)$ are shown in Figs. 1(c) and 1(d). The tilt forces only selective regions of the momentum space to be available for vertical transitions in region II, leading to a discontinuity in the optical response at the onset of region III.

B. $\sigma_{zz}(\omega)$

We calculate calculate $\sigma_{zz}(\omega)$ in a similar manner (see Appendix A for details of the calculation). For the case of the type-I WSM with $|\alpha_t| < 1$, the real part is given by

$$\mathrm{Re}[\sigma_{zz}(\omega)] = \begin{cases} 0, & \mathrm{I}: \ \omega < \omega_l, \\ \sigma_\omega \eta_4, & \mathrm{II}: \ \omega_l < \omega < \omega_u, \\ \sigma_\omega, & \mathrm{III}: \ \omega > \omega_u. \end{cases} \tag{17}$$

Here, we have defined

$$\eta_4 = \frac{1}{2} + \frac{(2\mu - \hbar\omega)^3}{4\hbar^3\omega^3|\alpha_t|^3} + \frac{1}{|\alpha_t|}\left(\frac{3}{4} - \frac{3\mu}{2\hbar\omega}\right). \tag{18}$$

For the type-II WSM, with $|\alpha_t| > 1$, we obtain [69]

$$\mathrm{Re}[\sigma_{zz}(\omega)] = \begin{cases} 0, & \mathrm{I}: \ \omega < \omega_l, \\ \sigma_\omega \eta_4, & \mathrm{II}: \ \omega_l < \omega < \omega_u', \\ \sigma_\omega \eta_5, & \mathrm{III}: \ \omega > \omega_u'. \end{cases} \tag{19}$$

Here, we have defined

$$\eta_5 = \frac{-1}{2|\alpha_t|^3}\left[1 - 3\alpha_t^2 + \frac{12\mu^2}{\hbar^2\omega^2}\right]. \tag{20}$$

The imaginary part of σ_{zz}, for a type-I WSM is calculated to be

$$\frac{\mathrm{Im}[\sigma_{zz}]}{\sigma_\omega} = \frac{-1}{2\pi}\left\{\tau'(\alpha_t)\ln\left[\frac{|\omega_u^2 - \omega^2|}{|\omega_l^2 - \omega^2|}\right] - \frac{8}{\alpha_t^2}\left(\frac{\mu}{\hbar\omega}\right)^2 + \left(\frac{\mu}{\hbar\omega}\right)^3 \Pi'(\mu,\omega,\alpha_t)\ln\left[\frac{|\omega_u - \omega|(\omega_l + \omega)}{|\omega_l - \omega|(\omega_u + \omega)}\right] \right.$$
$$\left. - \frac{6}{|\alpha_t|^3}\left(\frac{\mu}{\hbar\omega}\right)^2 \ln\left[\frac{|\omega_u^2 - \omega^2|\omega_l^2}{|\omega_l^2 - \omega^2|\omega_u^2}\right] + 2\ln\left[\frac{|\omega_c^2 - \omega^2|}{|\omega_u^2 - \omega^2|}\right]\right\}. \tag{21}$$

For a type-II WSM with $|\alpha_t| > 1$, we obtain

$$\frac{\mathrm{Im}[\sigma_{zz}]}{\sigma_\omega} = \frac{-1}{2\pi}\left\{\tau'(\alpha_t)\ln\left[\frac{|\omega_u'^2 - \omega^2|}{|\omega_l^2 - \omega^2|}\right] - \frac{8}{\alpha_t^3}\left(\frac{\mu}{\hbar\omega}\right)^2 + \left(\frac{\mu}{\hbar\omega}\right)^3 \Pi'(\mu,\omega,\alpha_t)\ln\left[\frac{|\omega_u' - \omega|(\omega_l + \omega)}{|\omega_l - \omega|(\omega_u' + \omega)}\right] \right.$$
$$\left. - \frac{6}{|\alpha_t|^3}\left(\frac{\mu}{\hbar\omega}\right)^2 \ln\left[\frac{|\omega_u'^2 - \omega^2|\omega_l^2}{|\omega_l^2 - \omega^2|\omega_u'^2}\right] + \left(\frac{-1}{\alpha_t^3} + \frac{3}{\alpha_t}\right)\ln\left[\frac{|\omega_c^2 - \omega^2|}{|\omega_u'^2 - \omega^2|}\right] - \frac{12}{|\alpha_t|^3}\left(\frac{\mu}{\hbar\omega}\right)^2 \ln\left[\frac{|\omega_c^2 - \omega^2|\omega_u'^2}{|\omega_u'^2 - \omega^2|\omega_c^2}\right]\right\}. \tag{22}$$

Here, we have defined

$$\tau'(\alpha_t) = \frac{1}{2}\left(2 - \frac{1}{|\alpha_t|^3} + \frac{3}{|\alpha_t|}\right), \tag{23}$$

$$\Pi'(\mu,\omega,\alpha_t) = \frac{4}{|\alpha_t|^3} + 3\left(\frac{\hbar\omega}{\mu}\right)^2\left(\frac{1}{|\alpha_t|^3} - \frac{1}{|\alpha_t|}\right). \tag{24}$$

The real and the imaginary parts of $\sigma_{zz}(\omega)$ are displayed in panels (e) and (f) of Fig. 1. We recall that region I is completely Pauli blocked while region II is partially Pauli blocked for vertical optical transitions.

C. $\sigma_{xy}(\omega)$

A finite transverse optical conductivity $\sigma_{xy}(\omega)$ generally originates from the breaking of the time-reversal symmetry. In the case of time reversal symmetry broken WSMs, this manifests in the separation (in momentum space) of the two Weyl nodes of opposite chirality. Thus the energy scale of the transverse optical response is dictated by the internode separation, $\epsilon_Q = \hbar v_F Q$.

The imaginary part of the dynamical transverse optical conductivity has already been calculated in Ref. [64], and our calculations (see Appendix B for details) reproduce their results. For a type-I WSM hosting a pair of oppositely tilted Weyl nodes with $|\alpha_t| < 1$, we obtain

$$\mathrm{Im}[\sigma_{xy}(\omega)] = \mathrm{sgn}(\alpha_t) \begin{cases} 0, & \mathrm{I}: \ \omega < \omega_l, \\ 3\sigma_\omega \eta_3, & \mathrm{II}: \ \omega_l < \omega < \omega_u, \\ 0, & \mathrm{III}: \ \omega > \omega_u. \end{cases} \tag{25}$$

Here we have defined

$$\eta_3 = \frac{1}{\alpha_t^2}\left(\frac{1}{8} - \frac{\mu}{2\hbar\omega} + \frac{\mu^2}{2\hbar^2\omega^2}\right) - \frac{1}{8}. \tag{26}$$

For a type-II WSM with a pair of oppositely tilted Dirac nodes with $|\alpha_t| > 1$, we derive

$$\mathrm{Im}[\sigma_{xy}(\omega)] = \mathrm{sgn}(\alpha_t) \begin{cases} 0, & \mathrm{I}: \ \omega < \omega_l, \\ 3\sigma_\omega \eta_3, & \mathrm{II}: \ \omega_l < \omega < \omega_u', \\ \frac{-3\mu\sigma_\omega}{\hbar\omega\alpha_t^2}, & \mathrm{III}: \ \omega > \omega_u'. \end{cases} \tag{27}$$

The real part of $\sigma_{xy}(\omega)$ can now be obtained by using Kramers-Kronig relations on $\mathrm{Im}[\sigma_{xy}(\omega)]$. In general we find

that $\mathrm{Re}[\sigma_{xy}(\omega)] = \mathrm{Re}[\sigma_{xy}^{dc}] + \mathrm{Re}[\sigma_{xy}^{ac}]$, where $\mathrm{Re}[\sigma_{xy}^{ac}(\omega \to 0)] \to 0$ and $\mathrm{Re}[\sigma_{xy}^{dc}(\omega = 0)]$ is finite.

For the case of a type-I WSM, we obtain the anomalous Hall component,

$$\mathrm{Re}\left[\sigma_{xy}^{dc}\right] = \sigma_Q + \sigma_\mu\left[\frac{2}{\alpha_t} + \frac{1}{\alpha_t^2}\ln\left(\frac{1-\alpha_t}{1+\alpha_t}\right)\right]. \tag{28}$$

Here we have defined a chemical potential based conductivity scale $\sigma_\mu = e^2\mu/(h^2 v_F)$ and a node separation based conductivity scale $\sigma_Q = e^2 Q/(\pi h)$. A similar calculation for the type-II WSM for the anomalous Hall component leads to

$$\mathrm{Re}\left[\sigma_{xy}^{dc}\right] = \frac{\sigma_Q}{|\alpha_t|} + \frac{\mathrm{sgn}(\alpha_t)\sigma_\mu}{\alpha_t^2}\ln\left[\frac{\mu^2}{\hbar^2\omega_c^2\alpha_t^2\left(\alpha_t^2-1\right)}\right]. \tag{29}$$

The ac component for a tilted type-I WSM is given by

$$\mathrm{Re}\left[\sigma_{xy}^{ac}\right] = \mathrm{sgn}(\alpha_t)\sigma_\mu\left\{\frac{-1}{2\alpha_t^2}\ln\left[\frac{|\omega_u^2-\omega^2|}{|\omega_l^2-\omega^2|}\frac{\omega_l^2}{\omega_u^2}\right] + \left(\frac{\mu}{2\hbar\omega\alpha_t^2} + \frac{\hbar\omega}{8\mu}\frac{1-\alpha_t^2}{\alpha_t^2}\right)\ln\left[\frac{|\omega_u-\omega|(\omega_l+\omega)}{|\omega_l-\omega|(\omega_u+\omega)}\right] - \frac{1}{|\alpha_t|}\right\}. \tag{30}$$

The corresponding ac component for a type-II WSM with a pair of oppositely tilted WSM nodes is given by

$$\mathrm{Re}\left[\sigma_{xy}^{ac}\right] = \mathrm{sgn}(\alpha_t)\sigma_\mu\left\{\frac{-1}{2\alpha_t^2}\ln\left[\frac{\left(\omega_c^2-\omega^2\right)^2}{|\omega_l^2-\omega^2||\omega_{u'}^2-\omega^2|}\frac{\omega_l^2\omega_{u'}^2}{\omega_c^4}\right] + \left(\frac{\mu}{2\hbar\omega\alpha_t^2} + \frac{\hbar\omega}{8\mu}\frac{1-\alpha_t^2}{\alpha_t^2}\right)\ln\left[\frac{|\omega_{u'}-\omega|(\omega_l+\omega)}{(\omega_{u'}+\omega)|\omega_l-\omega|}\right] - \frac{2}{\alpha_t^2}\right\}. \tag{31}$$

The first term of the anomalous Hall conductivity in Eqs. (28) and (29) is $\propto \sigma_Q$ and it denotes the "intrinsic contribution" which survives even if $\mu \to 0$. All other terms in the dc as well as the ac component of the off-diagonal conductivity ($\propto \sigma_\mu$) are "extrinsic contributions" which vanish in the limit $\mu \to 0$. The real and the imaginary parts of $\sigma_{xy}(\omega)$ for a type-I WSM are shown in Fig. 2, as a function of the optical frequency. The presence of the QAH contribution in the real part of σ_{xy} is evident. The imaginary part of σ_{xy} in Fig. 2 reverses sign upon changing the tilt orientation ($\alpha_t \to -\alpha_t$). Similar behavior is also observed in the corresponding plots for the type-II WSM (not shown here). The tilt dependence of $\sigma_{xy}(\omega)$ is highlighted in Fig. 3. In Fig. 3(a), the dominant contribution comes from the QAH part and consequently the curves for different frequencies are very close to each other. The intrinsic part of the QAH conductivity ($\propto \sigma_Q$) in turn dominates in the type-I WSM, while in the type-II WSM the α_t-dependent extrinsic part of the QAH ($\propto \sigma_\mu$) also contributes equally.

There are several previous works which calculate bits and parts of the optical conductivity matrix. However, most of the works do not discuss the most general situation, i.e., the

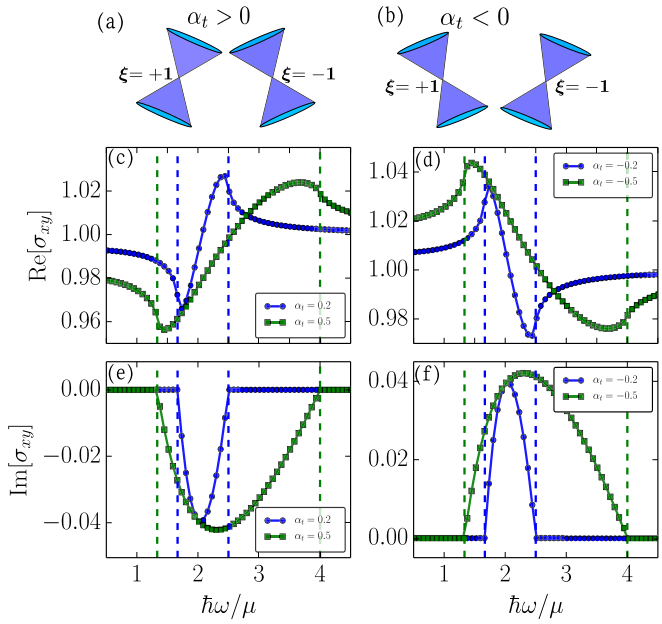

FIG. 2. (a), (b) The relative orientation of a pair of Weyl nodes for $\alpha_t > 0$ and for $\alpha_t < 0$, respectively. The sign of α_t becomes important in σ_{xy}. (c), (d) Real part of σ_{xy} for $\alpha_t > 0$ and $\alpha_t < 0$, respectively. Note that σ_{xy} has a finite dc component, denoting the presence of quantum anomalous Hall conductivity. (e), (f) Imaginary parts of σ_{xy} for $\alpha_t > 0$ and $\alpha_t < 0$, respectively. Evidently, $\mathrm{Im}[\sigma_{xy}] \propto \mathrm{sgn}(\alpha_t)$. Here, the conductivities are scaled in units of $\sigma_Q = e^2 Q/(\pi h)$, and other parameters are identical to those of Fig. 1.

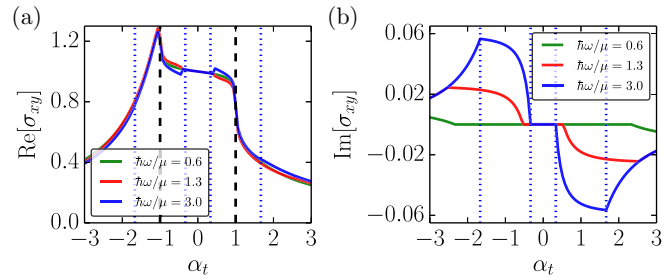

FIG. 3. The tilt (α_t) dependence of the (a) real and (b) imaginary part of σ_{xy} for different optical frequencies. The vertical black dashed lines simply mark $\alpha_t = \pm 1$. The vertical blue lines mark the boundary values for transition frequencies for regions I and II, i.e., $2\hbar^{-1}\mu/(|\alpha_t| \pm 1)$ for $\hbar\omega/\mu = 3.0$. The curves for $\hbar\omega/\mu = 0.6$ lie completely within the Pauli-blocked region, and thus they show only the QAH contribution. Clearly the behavior of the QAH term changes significantly across the Lifshitz transition ($|\alpha_t| = \pm 1$) line, dividing the type-I and type-II regions. All other parameters are identical to those of Fig. 2, and the conductivities are in units of σ_Q.

effect of tilt and finite μ for all frequency ranges. In contrast, we present the analytical results for the full complex optical conductivity matrix for tilted type-I and type-II WSMs. Having obtained the full conductivity matrix, we now discuss the polarization rotation of a reflected beam in tilted type-I and type-II WSMs, starting with the case of thin films in the next section. The finite off-diagonal components of the conductivity matrix (σ_{xy}) will play an important role in the polarization rotation of the reflected (and transmitted) light and the corresponding ellipticity angle in WSM thin films. Note that we have not explicitly considered the impact of intraband optical transitions which appear as Drude contributions (peaked at $\omega = 0$) to the longitudinal components of the conductivity matrix (σ_{xx}, σ_{yy}, and σ_{zz}). Including these Drude terms in our calculations will quantitatively change some results in the $\omega \to 0$ regime, while not having a significant effect in the finite ω (optical) regime.

IV. KERR ROTATION IN THIN FILMS OF WSMs

In this section, we consider an ultrathin film of a Weyl semimetal such that the thickness of the film (d) is much larger than the atomic separation (a) while being smaller than the wavelength (λ) of light, i.e., $a \ll d \ll \lambda$. In these conditions the WSM film can be treated as a 2D surface, as far as its interaction with light is concerned. Thus the polarization angle rotation can be obtained simply by matching the electromagnetic boundary conditions on either side of the thin film.

The polarization angle $\Phi_{\rm Kerr}$ and the azimuth of the major axes of the polarization ellipse $\Psi_{\rm Kerr}$ (ellipticity angle) of the reflected beam are given by Eq. (6). We need to distinguish between the two cases of the incident beam being s (polarization $\parallel$ to the plane of incidence) or p (polarization $\perp$ to the plane of incidence) polarized. For the case of a reflected beam, the corresponding dimensionless complex quantities [χ of Eq. (6)] are defined as

$$\chi^s_{\rm Kerr} = \frac{r_{ps}}{r_{ss}} \quad \text{and} \quad \chi^p_{\rm Kerr} = -\frac{r_{sp}}{r_{pp}}, \tag{32}$$

where r_{ij} with $(i, j) \in (s, p)$ are the corresponding reflection coefficients [67]. For thin films ($d \ll \lambda$), these reflection coefficients, in turn, depend on the *surface* conductivity matrix. In the case of a WSM, the surface conductivity matrix depends on the incident surface. For example, in a time reversal symmetry broken WSM, the surface conductivity has finite off-diagonal terms for the surface without Fermi arc states (surfaces $\perp \boldsymbol{Q}$) while it is diagonal for the surface hosting Fermi arcs states (surfaces $\parallel \boldsymbol{Q}$). We consider these two cases separately in the following subsections.

A. Incidence on surface without Fermi arc states ($\perp$ Q)

Let us start with the case where the linearly polarized incident beam propagates (say in direction $\hat{\mathbf{n}}$) parallel to $\boldsymbol{Q}$. In this case, both $\hat{\mathbf{n}}$ and $\boldsymbol{Q}$ are in the z direction and the electric polarization is in the x-y plane, and thus the transverse conductivity σ_{xy} will come into play.

Let us assume that the interface of air and WSM thin film is located at the $z = 0$ plane. The wave vectors for the initial, reflected, and transmitted beam are

$$\mathbf{k}_i = (0, k_i \sin\theta_i, k_i \cos\theta_i),$$
$$\mathbf{k}_r = (0, k_r \sin\theta_r, -k_r \cos\theta_r),$$
$$\mathbf{k}_t = (0, k_t \sin\theta_t, k_t \cos\theta_t).$$

Similarly the components of electric field $\mathbf{E}$ are

$$\mathbf{E}_i = \left(E_i^s, E_i^p \cos\theta_i, -E_i^p \sin\theta_i\right) e^{(\mathbf{k_i}\cdot\mathbf{r}-\omega_i t)},$$
$$\mathbf{E}_r = \left(E_r^s, E_r^p \cos\theta_r, E_r^p \sin\theta_r\right) e^{(\mathbf{k_r}\cdot\mathbf{r}-\omega_r t)},$$
$$\mathbf{E}_t = \left(E_t^s, E_t^p \cos\theta_t, -E_t^p \sin\theta_t\right) e^{(\mathbf{k_t}\cdot\mathbf{r}-\omega_t t)}.$$

The magnetic field $\mathbf{B}$ components can be simply obtained via $\mathbf{B} = (n/c)\hat{\mathbf{k}} \times \mathbf{E}$, with n denoting the refractive index of the medium. The fields on the two sides of the WSM thin film are connected by the Maxwell boundary condition:

$$\mathbf{E}_1^{||} = \mathbf{E}_2^{||} \quad \text{and} \quad \hat{\mathbf{n}} \times \left(\frac{\mathbf{B}_1^{||}}{\mu_1} - \frac{\mathbf{B}_2^{||}}{\mu_2}\right) = \mathbf{J}, \tag{33}$$

where $\mathbf{E}_1 = \mathbf{E}_i + \mathbf{E}_r$, $\mathbf{E}_2 = \mathbf{E}_t$, $\mathbf{B}_1 = \mathbf{B}_i + \mathbf{B}_r$, $\mathbf{B}_2 = \mathbf{B}_t$, and $\mathbf{J}$ is the surface current density generated by the incident electric field. The surface current density can be expressed in terms of the surface conductivity matrix, $J_i = \sigma^s_{ij} E_j$. The surface conductivity for a thin film of thickness d can be approximated as $\sigma^s_{ij} = d\,\sigma_{ij}$, with σ_{ij} denoting the bulk conductivity [47].

In general, the reflected electric field in the p and s directions can be expressed as

$$\begin{pmatrix} E_r^p \\ E_r^s \end{pmatrix} = \begin{pmatrix} r_{pp} & r_{ps} \\ r_{sp} & r_{ss} \end{pmatrix} \begin{pmatrix} E_i^p \\ E_i^s \end{pmatrix}. \tag{34}$$

Using this in Eq. (33), we obtain the reflection coefficients as

$$r_{sp} = \left.\frac{E_r^s}{E_i^p}\right|_{E_i^s=0} = \frac{2n_i}{c\mu_i} \frac{\sigma^s_{xy} \cos\theta_i \cos\theta_t}{\left(\sigma^s_{xy}\sigma^s_{yx} \cos\theta_i \cos\theta_t - \sigma_1^s \sigma_2^s\right)}, \tag{35}$$

$$r_{ss} = \left.\frac{E_t^s}{E_i^s}\right|_{E_i^p=0} = -1 + \frac{2n_i}{c\mu_i}\left[\frac{\sigma_2^s \cos\theta_i}{\sigma_1^s\sigma_2^s - \sigma^s_{xy}\sigma^s_{yx} \cos\theta_i \cos\theta_t}\right], \tag{36}$$

along with

$$r_{pp} = \left.\frac{E_t^p}{E_i^p}\right|_{E_i^s=0} = -1 + \frac{2n_i}{c\mu_i}\left[\frac{\sigma_1^s \cos\theta_t}{\sigma_1^s\sigma_2^s - \sigma^s_{xy}\sigma^s_{yx} \cos\theta_i \cos\theta_t}\right] \tag{37}$$

and

$$r_{ps} = \left.\frac{E_r^p}{E_i^s}\right|_{E_i^p=0} = \frac{2n_i}{c\mu_i} \frac{\sigma^s_{yx} \cos\theta_i \cos\theta_t}{\left(\sigma^s_{xy}\sigma^s_{yx} \cos\theta_i \cos\theta_t - \sigma_1^s \sigma_2^s\right)}. \tag{38}$$

Here, we have defined $\sigma_1^s \equiv n_i \cos\theta_i/(c\mu_i) + n_t \cos\theta_t/(c\mu_t) + \sigma^s_{xx}$ and $\sigma_2^s \equiv n_i \cos\theta_t/(c\mu_i) + n_t \cos\theta_i/(c\mu_t) + \sigma^s_{yy} \cos\theta_i \cos\theta_t$.

Clearly, the reflectivity coefficients that rotate the incoming polarization, r_{sp} and r_{ps}, are proportional to the optical Hall conductivity and they vanish in the limit of $\sigma^s_{xy} \to 0$. In our case we find that $\sigma^s_{xy} = -\sigma^s_{yx}$ and thus $r_{sp} = -r_{ps}$. Furthermore for normal incidence we have $\theta_i = \theta_t = 0$ and thus $\sigma_1 = \sigma_2$ and $r_{ss} = r_{pp}$. As a consequence, for the case of normal incidence, we have $\Phi_s = \Phi_p$ [70].

As a consistency check, we note that for an isotropic WSM without any tilt, and for the case of normal incidence

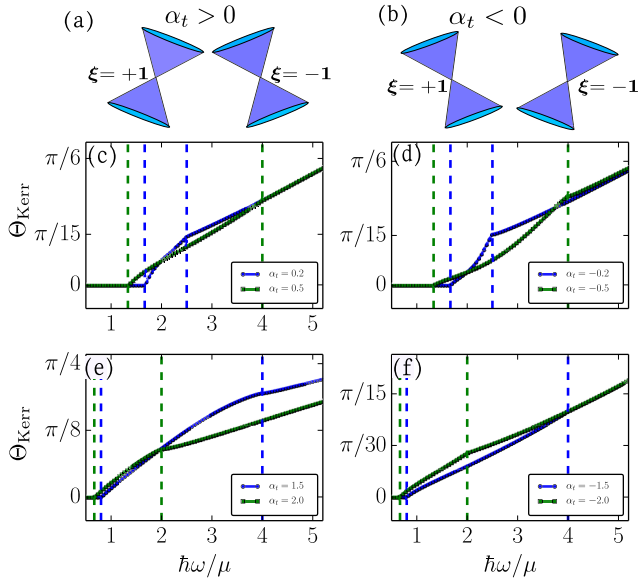

FIG. 4. (a), (b) The relative orientation of a pair of Weyl nodes for $\alpha_t > 0$ and for $\alpha_t < 0$, respectively. The giant Kerr angle of the reflected optical beam as a function of the optical frequency for (c) type-I WSMs with $\alpha_t > 0$, (d) type-II WSMs with $\alpha_t < 0$, (e) type-II WSMs with $\alpha_t > 0$, (f) type-II WSMs with $\alpha_t < 0$. The scale of the GKR is fixed by the ratio $\sigma_{xy}/\sigma_{xx} \propto v_F Q/\omega$. Thus in crystalline systems, GKR of the order of a radian can be observed for $\omega \approx 10^{14}$ rad/s, and appropriate choice of μ. The dashed vertical lines show the boundaries of region I and region II for the corresponding α_t. Here we have chosen $\mu = 0.125$ eV and $Q = 10^8$ m^{-1}, $d = 10$ nm; $\Theta_{\rm Kerr}$ is in radians.

$(\theta_i = \theta_t = 0)$, we recover the results of Ref. [47]. For the case of normal incidence, using Eq. (35)–(38) in Eq. (32), we obtain

$$\chi^p_{\rm Kerr} = -\frac{\sigma_{xy}}{\sigma_{xx}}\left[1 + \frac{d\sigma_{xx}}{2c\epsilon_0}\left(1 + \frac{\sigma^2_{xy}}{\sigma^2_{xx}}\right)\right]^{-1}. \tag{39}$$

This establishes that $\chi^p_{\rm Kerr} \propto Q$, to lowest order in Q, as $\sigma_{xy} \propto Q$, and σ_{xx} is independent of Q. The polarization rotation is primarily determined by the ratio of σ_{xy}/σ_{xx}, and we get giant polarization rotation for $\sigma_{xy}/\sigma_{xx} \approx 1$, or alternately $\sigma_Q/\sigma_\omega = 6Qv_F/(\pi\omega) \approx 1$. In a typical WSM, we have $Q \approx 10^8$ m^{-1} (for example, $Q = 3.2 \times 10^8$ m^{-1} in WTe_2 [11]), and $v_F \approx 10^6$ m/s. Thus $\omega \approx 10^{14}$ rad/s or smaller is needed for observing the GKR in WSM thin films. In the other term in the denominator we have $d\sigma_{xx}/(c\epsilon_0) \approx \alpha_F \omega d/(3v_F) = (2\pi\alpha_F c/v_F)(d/\lambda)$, where $\alpha_F = e^2/4\pi\hbar c\epsilon_0 \approx 1/137$ is the fine-structure constant. Since $2\pi\alpha_F c/v_F$ is of $O(1)$ and we are working in $d/\lambda \ll 1$, the d dependence of $\chi^p_{\rm Kerr}$ in WSM thin films is insignificant. In this limit of $d/\lambda \ll 1$, the d dependence of Eq. (39) drops out, and the Kerr angle can be expressed as

$$\tan(2\Theta_{\rm Kerr}) = -2\,\frac{{\rm Re}[\sigma_{xy}]{\rm Re}[\sigma_{xx}] + {\rm Im}[\sigma_{xy}]{\rm Im}[\sigma_{xx}]}{|\sigma_{xx}|^2 - |\sigma_{xy}|^2}. \tag{40}$$

The dependence of the Kerr angle of rotation for normal incidence on a freestanding tilted WSM thin film ($n_i = n_t \approx 1$ and $\theta_i = \theta_t$) is shown in Fig. 4. As opposed to the typical values of microradians in ferromagnetic systems and topological insulators, in WSMs the GKR can be on the order of a radian for a reasonable choice of parameters. Furthermore, two distinct kinks in the GKR should be observable upon scanning the optical frequencies (or the chemical potential/doping) across the Pauli blocking of region I and region II in tilted WSMs. A similar behavior will also be seen in the ellipticity angle measurement (not shown here).

B. Incidence on surface with Fermi arcs states ($\parallel$ Q)

In this scenario, light propagates ($\hat{\mathbf{n}}$) perpendicular to the z axis, and the polarization of the incident electric field is in the y-z (or x-z) plane. Consequently, the polarization rotating off diagonal reflection coefficients is

$$r_{sp} \propto \sigma_{zy} = 0 \quad \text{or} \quad r_{sp} \propto \sigma_{zx} = 0. \tag{41}$$

Consequently, in this case there is no polarization rotation. This offers an optical probe to distinguish the surfaces of a WSM which host Fermi arc surface states.

V. KERR ROTATION IN SEMI-INFINITE WSMs

Having explored the polarization rotation in thin films of WSMs, we now focus on the polarization rotation due to a semi-infinite slab of a WSM. In the bulk of a WSM, the Maxwell equations are themselves modified by the presence of an axionic term [47,54,55]. This axionic term, in turn, has important consequences in the polarization rotation of the reflected light [47]. It also results in the topological magnetoelectric effect [71] which has been recently studied in topological insulators and WSMs. As opposed to the case of topological insulators, where the axion field is a constant, the axion field in WSMs has a nontrivial dependence on space and time owing to the breaking of time-reversal and inversion symmetries.

The axionic term is added to the Lagrangian of the electromagnetic field [54] via the following term, $\delta\mathcal{L} = c\epsilon_0\alpha_F\vartheta\boldsymbol{E}\cdot\boldsymbol{B}/\pi$, with α_F being the fine-structure constant, and ϑ the axionic field. In a WSM, we have $\vartheta(\boldsymbol{r},t) = 2\boldsymbol{Q}\cdot\boldsymbol{r} - 2\mathcal{Q}_0 t$, with $\mathcal{Q}_0$ ($\boldsymbol{Q}$) denoting the separation of the two Weyl nodes in the energy (momentum) space. For a WSM with inversion symmetry we have $\mathcal{Q}_0 = 0$. In materials exhibiting the axionic response, the electric polarization and magnetization have additional contributions arising from the topological terms [23,54],

$$\boldsymbol{D} = \boldsymbol{\epsilon}\boldsymbol{E} + c\epsilon_0\alpha_F\vartheta\boldsymbol{B}/\pi, \tag{42}$$

$$\boldsymbol{H} = \boldsymbol{B}/\mu_p - c\epsilon_0\alpha_F\vartheta\boldsymbol{E}/\pi. \tag{43}$$

Here $\boldsymbol{\epsilon}$ is the dielectric matrix and μ_p is the permeability.

Accordingly, the Maxwell equation for the electric field propagation in a WSM is modified to be

$$\nabla^2\boldsymbol{E} - \boldsymbol{\nabla}(\boldsymbol{\nabla}\cdot\boldsymbol{E}) = \frac{1}{c^2\epsilon_0}\frac{\partial(\boldsymbol{\sigma}\cdot\boldsymbol{E})}{\partial t} + \frac{\epsilon_b}{c^2}\frac{\partial^2\boldsymbol{E}}{\partial t^2} + \frac{2\alpha_F}{\pi c}\boldsymbol{Q}\times\frac{\partial\boldsymbol{E}}{\partial t}. \tag{44}$$

Here we have assumed the relative permeability (μ_p/μ_{p0}) to be unity, and ϵ_b is the static relative permittivity arising from the bound charge polarization. See Appendix C for details of the derivation of Eq. (44). For the case of a bulk WSM,

with $d \gg \lambda$, the last term in Eq. (44) plays an important role in obtaining the Fresnel coefficients. Again, we need to distinguish between the two cases when the light is incident on the surface hosting Fermi arc surface states ($\hat{\mathbf{n}} \perp \boldsymbol{Q}$) and on a surface without the Fermi arc states ($\hat{\mathbf{n}} \parallel \boldsymbol{Q}$). We show that these two cases qualitatively correspond to the Faraday and Voigt geometries discussed in the context of magneto-optic effects in magnetic systems such as (Ga,Mn)As [56]. In a time reversal symmetry broken WSM, $\boldsymbol{Q}$ acts analogously to magnetization in a ferromagnet, whose relative orientation with respect to $\hat{\mathbf{n}}$ results in different effects described below.

A. Incidence on surface without Fermi arc states

Let us consider a normal incidence of light on a surface without Fermi arcs, i.e., $\hat{\mathbf{n}} \parallel \boldsymbol{Q} = Q\hat{z}$. In this case we have $\boldsymbol{Q} \cdot \boldsymbol{B} = 0$, and consequently the axion charge density, $\rho_\vartheta = -2\alpha_F c\epsilon_0 \boldsymbol{Q} \cdot \boldsymbol{B}/\pi = 0$ [see Eq. (C3) in Appendix C for details]. Here, $\boldsymbol{Q}$ plays the role of effective magnetization, and light propagates parallel to it. This setting is similar to that of "Faraday geometry," which results in the magneto-optic polar Kerr effect in magnetic materials [72].

The propagation of light inside the WSM along the $\hat{z}$ direction can be obtained from Eq. (44), as detailed in Appendix C. It is described by the following matrix equation,

$$n^2 \begin{pmatrix} E_x \\ E_y \\ 0 \end{pmatrix} = \begin{pmatrix} \epsilon'_{xx} & \epsilon'_{xy} & 0 \\ -\epsilon'_{xy} & \epsilon'_{yy} & 0 \\ 0 & 0 & \epsilon'_{zz} \end{pmatrix} \begin{pmatrix} E_x \\ E_y \\ E_z \end{pmatrix}. \tag{45}$$

Here, n denotes the complex refractive index, and ϵ'_{ij} is the complex dielectric function including the axion terms. The elements of ϵ'_{ij} are readily expressed in terms of the optical conductivities and the internode separation as [47,73] $\epsilon'_{yy} = \epsilon'_{xx}$, where

$$\epsilon'_{xx} = \epsilon_b + \frac{i}{\omega\epsilon_0}\sigma_{xx} \quad \text{and} \quad \epsilon'_{zz} = \epsilon_b + \frac{i}{\omega\epsilon_0}\sigma_{zz}. \tag{46}$$

The off-diagonal element of ϵ'_{xy} is what typically leads to optical activity, and it is given by

$$\epsilon'_{xy} = \frac{i}{\omega\epsilon_0}\sigma_{xy} + \frac{2i\alpha_F c}{\pi}\frac{Q}{\omega} = \frac{i}{\omega\epsilon_0}(\sigma_{xy} + \sigma_Q). \tag{47}$$

Here, α_F is the fine-structure constant, and σ_{ij} are the complex optical conductivities.

Interestingly, Eq. (47) comprises two terms, one resulting from finite transverse conductivity and the other owing its origin solely to the axionic term and modified dynamics of the electromagnetic waves. This "gyrotropic" term is not present in the conventional definition of the dielectric constant in metals: $\epsilon_{ij}(\omega) = \delta_{ij}\epsilon_b + i\sigma_{ij}(\omega)/\epsilon_0\omega$. The dielectric constant can also be expressed as $\epsilon'_{ij} = \epsilon_{ij} + \varepsilon_{ijk}Q_k \times 2i\alpha_F c/(\pi\omega)$, where ε_{ijk} is the antisymmetric Levi-Civita tensor, and Q_k denotes the kth component of the Weyl node separation vector $\boldsymbol{Q}\,(= Q\hat{z})$. Thus, the gyrotropic constant in WSMs $\propto Q/\omega$, making its optical response analogous in spirit to that of magnetic materials. The real and the imaginary parts of the different components of the modified dielectric tensor are shown in Fig. 5. The axionic term in $\mathrm{Im}(\epsilon'_{xy}) \propto Q/\omega$ makes it diverge in the low-frequency regime. This will lead to anomalous optical activity even in the low-frequency, Pauli-blocked regime. Notice that in Fig. 5, $\mathrm{Im}(\epsilon'_{xx}) \ll \mathrm{Re}(\epsilon'_{xx})$, $\mathrm{Im}(\epsilon'_{zz}) \ll \mathrm{Re}(\epsilon'_{zz})$, and $\mathrm{Re}(\epsilon'_{xy}) \ll \mathrm{Im}(\epsilon'_{xy})$.

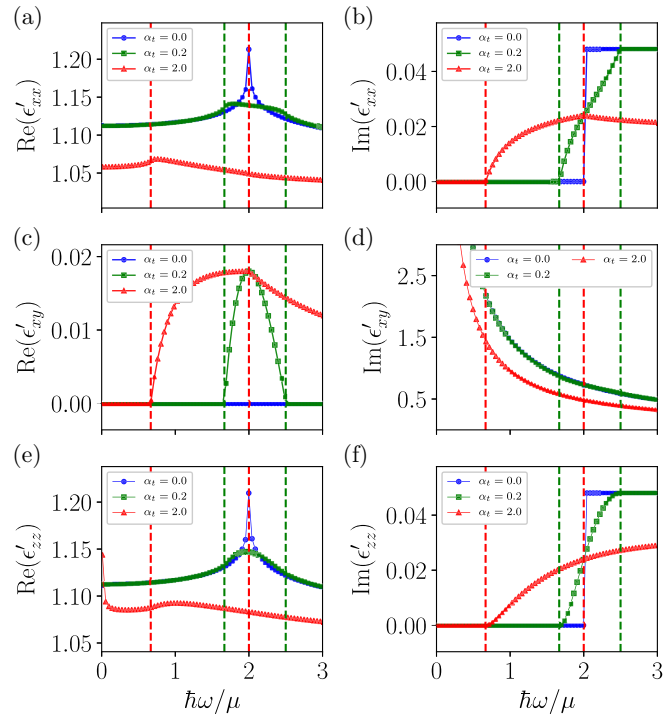

FIG. 5. The optical frequency dependence of the real and imaginary parts of the effective dielectric matrix ϵ'_{ij} (including the axion term) for different tilt parameters. (a) $\mathrm{Re}(\epsilon'_{xx})$, (b) $\mathrm{Im}(\epsilon'_{xx})$, (c) $\mathrm{Re}(\epsilon'_{xy})$, (d) $\mathrm{Im}(\epsilon'_{xy})$, (e) $\mathrm{Re}(\epsilon'_{zz})$, (f) $\mathrm{Im}(\epsilon'_{zz})$. The axion term appears in $\mathrm{Im}(\epsilon'_{xy}) \propto Q/\omega$, making it diverge in the low-frequency regime. The vertical dashed lines mark the boundary of regions I and II for $\alpha_t = 0.2$ in green and $\alpha_t = 2$ in red. Here we have chosen $\epsilon_b = 1$ and other parameters are identical to those of Fig. 4.

Equation (45) permits nontrivial solution for the electromagnetic fields only for the following conditions [72]:

$$n_+^2 = \epsilon'_{xx} + i\epsilon'_{xy} \quad \text{and} \quad n_-^2 = \epsilon'_{xx} - i\epsilon'_{xy}. \tag{48}$$

Here, n_+ and n_- are refractive indices of the left and right circularly polarized eigenmodes in the WSM. This becomes immediately clear upon substituting the two solutions obtained in Eq. (48) in (C11), which yield $\boldsymbol{E}_x = \pm i\boldsymbol{E}_y$. The real (imaginary) part of the difference, $\delta n = n_+ - n_-$, leads to circular birefringence (circular dichroism).

A finite δn solely arises from the $\epsilon'_{xy} \propto Q$ term (as $\sigma_{xy} \propto Q$), has both real and imaginary terms, and vanishes in the $Q \to 0$ limit.

Now the Fresnel reflection coefficient corresponding to these modes can be obtained via the well-known relation,

$$r_\pm = (1 - n_\pm)/(1 + n_\pm). \tag{49}$$

Here, the dimensionless constant χ_{PKE} is defined as

$$\chi_{\mathrm{PKE}} = i\frac{r_+ - r_-}{r_+ + r_-} = i\frac{n_+ - n_-}{n_+ n_- - 1}. \tag{50}$$

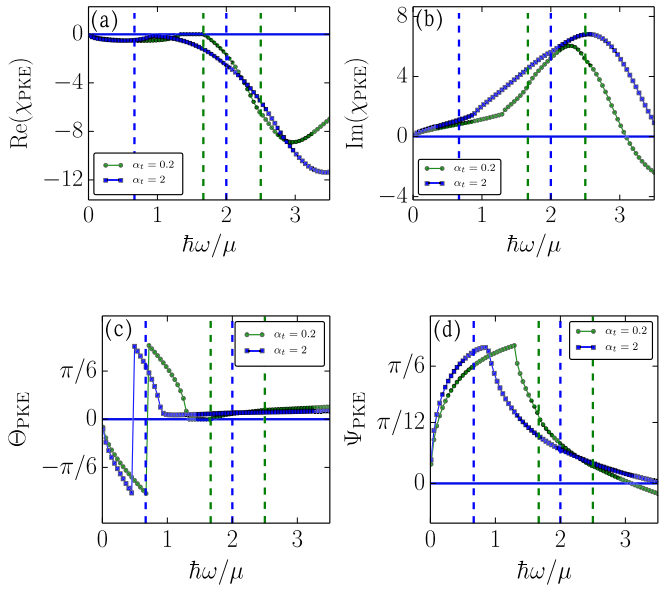

FIG. 6. (a) The real and (b) imaginary part of χ_{PKE}, as a function of the incident photon energy, for a semi-infinite slab of type-I and type-II WSMs. The resulting (c) giant polar Kerr effect (Θ_{PKE}), and ellipticity angle (Ψ_{PKE}), in radians. In this Faraday geometry, light propagates along the direction of the Weyl node separation, with large circular birefringence and dichroism. The solid horizontal line in both (c) and (d) shows the vanishing small optical activity if the axion term is neglected. Thus the optical activity is caused predominantly by the axion term. Interestingly, it should be observable also in the Pauli-blocked region where no optical transitions are allowed. Here, all the parameters are identical to those of Fig. 5.

This can be further simplified to obtain

$$\chi_{\mathrm{PKE}} = \frac{i\left(-\sqrt{\epsilon'_{xx} - i\epsilon'_{xy}} + \sqrt{\epsilon'_{xx} + i\epsilon'_{xy}}\right)}{-1 + \sqrt{\epsilon'_{xx} - i\epsilon'_{xy}}\sqrt{\epsilon'_{xx} + i\epsilon'_{xy}}}. \tag{51}$$

As opposed to the thin-film WSM geometry, where the polarization rotation solely arises due to a finite σ_{xy}, in bulk WSM, the axion term appearing in ϵ'_{xy} also plays an important role. Similarly to the magneto-optic polar Kerr effect which is odd in the magnetization [72], the polarization rotation here also is an odd function of Q. This can be seen from the exact Eq. (50), where the numerator is an odd function of Q and the denominator is an even function of Q. Furthermore, this can also be seen from the limiting case of $|\epsilon'_{xy}| \ll |\epsilon'_{xx}|$, for which Eq. (50) reduces to

$$\chi_{\mathrm{PKE}} \approx \frac{\epsilon'_{xy}}{(1 - \epsilon'_{xx})\sqrt{\epsilon'_{xx}}}. \tag{52}$$

The exact polarization rotation (Θ_{PKE}) and ellipticity angle (Ψ_{PKE}) can be obtained by using Eq. (50) in Eq. (6). The real and imaginary parts of χ_{PKE} and the resulting angles are shown in Fig. 6. Note the abrupt change in the sign of Θ_{PKE} in Fig. 6(c), in the Pauli-blocked regime. This is a consequence of $|\chi_{\mathrm{PKE}}| \to 1$ at the sign-reversal point, so that the $1 - |\chi_{\mathrm{PKE}}|^2$ in the denominator for the expression of Θ_{PKE} and Θ_{PKE} also flips sign. We emphasize that (1) the optical activity is predominantly caused by the axion term, and (2) it persists even in the Pauli-blocked frequency regime with no optical transitions.

In Fig. 6 we have chosen $\epsilon_b = 1$ to be of the same order as the conductivities in the optical regime. However in real materials ϵ_b can be larger. For example, it is 6.2 in type-I WSM TaAs [51] and has an even larger value of $\epsilon_b = 70$ in type-II WSM [74] WTe_2. For such large values of ϵ_b, in the optical regime we have $|\epsilon_{xx}| \gg |\epsilon_{xy}|$, and χ_{PKE} becomes small [see Eq. (52)] and real. Consequently the polarization angle also becomes vanishingly small for very large ϵ_b.

B. Incidence on surface with Fermi arc states

As we have fixed the momentum space separation of the two Weyl nodes to be in the z direction, the Fermi arc surface states appear on the surfaces parallel to the x-z or the y-z plane. For definiteness we consider the light propagating in the x direction, and incident on the surface parallel to y-z plane. Thus we have $\hat{\boldsymbol{n}} = \hat{\boldsymbol{x}}$ and $\hat{\boldsymbol{n}} \perp \boldsymbol{Q}$ (recall that $\boldsymbol{Q} = Q\hat{\boldsymbol{z}}$). This setting is similar to that of the "Voigt" geometry for polarization rotation in magnetic materials.

In this case, for wave propagation in the $\hat{\boldsymbol{x}}$ direction, Eq. (44) leads to (see Appendix C 2 for details of the calculation)

$$n^2 \begin{pmatrix} 0 \\ E_y \\ E_z \end{pmatrix} = \begin{pmatrix} \epsilon'_{xx} & \epsilon'_{xy} & 0 \\ -\epsilon'_{xy} & \epsilon'_{yy} & 0 \\ 0 & 0 & \epsilon'_{zz} \end{pmatrix} \begin{pmatrix} E_x \\ E_y \\ E_z \end{pmatrix}. \tag{53}$$

Here the effective dielectric constants have been defined in Eqs. (46) and (47). Similarly to the case of Eq. (45), Eq. (53) also permits two solutions for specific values of the refractive index,

$$n_\parallel^2 = \epsilon'_{zz} \quad \text{and} \quad n_\perp^2 = \epsilon'_{yy} - \frac{\epsilon'^2_{xy}}{\epsilon'_{xx}}, \tag{54}$$

which defines two linearly polarized modes: one traveling parallel to $\boldsymbol{Q}$, and another in the plane perpendicular to $\boldsymbol{Q}$. Note that $n_\perp^2$ is an even function of Q (of the form $a + bQ^2$, where both a and b are complex), while $n_\parallel^2$ is almost independent of Q. Consequently, $n_\perp$ is an even function of Q. The real (imaginary) part of the difference, $\delta n = n_\parallel - n_\perp$ leads to linear birefringence (linear dichroism). The electric field corresponding to these modes is given by $\boldsymbol{E}_\parallel = E_0\hat{\boldsymbol{z}}e^{i\omega(t \mp n_\parallel x/c)}$ and $\boldsymbol{E}_\perp = E_0(\hat{\boldsymbol{y}} + \hat{\boldsymbol{x}}\epsilon'_{xy}/\epsilon'_{xx})e^{i\omega(t \mp n_\perp x/c)}$, E_0 being the electric field amplitude. Analogous to the propagation of light in a Voigt geometry in a magnetic material, here also an electric field component parallel to the propagation direction ($E_x \propto \epsilon'_{xy}$) is also allowed.

Now let us consider the reflection of a linearly polarized optical beam from the infinite WSM slab. For an arbitrary incident polarization making an angle Θ_0 with respect to $\boldsymbol{Q}$, the electric field can be decomposed as

$$E_\parallel = E_I \cos(\Theta_0), \quad E_\perp = E_I \sin(\Theta_0). \tag{55}$$

Thus, the initial polarization angle with respect to $\boldsymbol{Q}$ can be expressed as $\Theta_0 = \tan^{-1}(E_\perp/E_\parallel)$. The beam becomes elliptically polarized upon reflection from the WSM slab. The corresponding χ_{Voigt}, which determines the ellipticity and

polarization angle, is given by

$$\chi_{\text{Voigt}} = \frac{r_\perp E_\perp}{r_\parallel E_\parallel} = \frac{r_\perp}{r_\parallel}\tan(\Theta_0). \tag{56}$$

Here $r_\parallel$ and $r_\perp$ are the Fresnel reflection coefficients for the parallel and perpendicular components, respectively. These are given by

$$r_{\parallel/\perp} = (1 - n_{\parallel/\perp})/(1 + n_{\parallel/\perp}). \tag{57}$$

As $n_\perp$ is an even function of Q, $r_\perp$ is also an even function of Q, while $r_\parallel$ is almost independent of Q. Consequently χ_{Voigt} and the resulting polarization rotation are also even functions of Q. This quadratic in Q polarization rotation in WSM is analogous to the Voigt effect, which is also termed the quadratic polar Kerr effect, or magnetic linear dichroism. Equation (56) can be further simplified to obtain

$$\chi_{\text{Voigt}} = \frac{\left(1 + \sqrt{-\frac{\epsilon'^2_{xy}}{\epsilon'_{xx}} + \epsilon'_{xx}}\right)\left(-1 + \sqrt{\epsilon'_{zz}}\right)}{\left(-1 + \sqrt{-\frac{\epsilon'^2_{xy}}{\epsilon'_{xx}} + \epsilon'_{xx}}\right)\left(1 + \sqrt{\epsilon'_{zz}}\right)}\tan(\Theta_0). \tag{58}$$

The polarization (Θ_{Voigt}) and ellipticity (Ψ_{Voigt}) angle of the reflected beam are easily calculated by substituting χ_{Voigt} in Eq. (6). For the case of $\Theta_0 = 0$ or π, i.e., the incident polarization aligned along $\boldsymbol{Q}$, we have $\chi_{\text{Voigt}} = 0$, and there is no polarization rotation. The reflected beam only suffers a phase change. For the general case, the relative polarization rotation angle $\delta_{\text{Voigt}} = \Theta_{\text{Voigt}} - \Theta_0$ can now calculated via the relation

$$\tan(2\delta_{\text{Voigt}}) = \frac{\tan(2\Theta_{\text{Voigt}}) - \tan(2\Theta_0)}{1 + \tan(2\Theta_{\text{Voigt}})\tan(2\Theta_0)}. \tag{59}$$

For the limiting case of $\Theta_0 = \pi/4$, Eq. (59) reduces to $\delta_{\text{Voigt}} = \pi/2 + 2\Theta_{\text{Voigt}}$. In another limiting case of $r_\perp/r_\parallel$ being real (as in the case of magnetic systems [68]), we obtain $\tan(\Theta_{\text{Voigt}}) = r_\perp \tan(\Theta_0)/r_\parallel$, and Eq. (59) reduces to the known result [68]

$$\tan(\delta_{\text{Voigt}}) = \frac{(r_\parallel - r_\perp)\tan(\Theta_0)}{r_\parallel + r_\perp \tan^2\Theta_0}. \tag{60}$$

Furthermore if $r_\parallel/r_\perp \approx 1$, Eq. (60) reduces to $\delta_{\text{Voigt}} \approx 0.5(r_\perp/r_\parallel - 1)\sin(2\Theta)$.

Figure 7 shows the dependence of the real and imaginary parts of χ_{Voigt}, along with Θ_{Voigt} and Ψ_{Voigt}, as a function of the optical frequency. Notice the existence of finite Θ_{Voigt} even in the Pauli-blocked regime. However in contrast to the Faraday geometry, here the ellipticity angle vanishes in the Pauli-blocked regime. Note that in Fig. 7, we have chosen $\epsilon_b = 1$. For systems with a very large values of ϵ_b, we have $|\epsilon_{zz}|, |\epsilon_{xx}| \gg |\epsilon_{xy}|$ and Eq. (58) yields $\chi_{\text{Voigt}} \to \tan(\Theta_0)$, leading to $\Theta_{\text{Voigt}} \to \Theta_0$ and $\delta_{\text{Voigt}} \to 0$. Thus a type-I WSM with a relatively small dielectric constant is more suitable for observing the proposed polarization rotation in the optical regime.

In all our discussion till now, we have restricted ourselves to a time reversal symmetry broken WSM, with both the Weyl nodes being at the same chemical potential. Our results can easily be generalized to include inversion symmetry broken

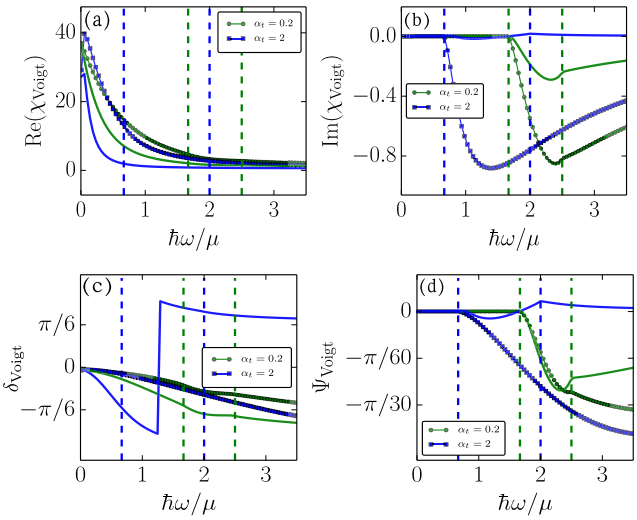

FIG. 7. (a) The real and (b) imaginary part of χ_{Voigt}, as a function of the incident photon energy, for a semi-infinite slab of type-I and type-II WSMs. The resulting (c) polarization rotation (or Voigt effect, $\delta_{\text{Voigt}} = \Theta_{\text{Voigt}} - \Theta_0$), and (d) ellipticity angle (Ψ_{Voigt}), in radians. In this Voigt geometry, light propagates perpendicular to the Weyl node separation, with large linear birefringence and dichroism. The solid lines in both (c) and (d) show the corresponding optical activity if the axion term is neglected. Notice that unlike the case of Faraday geometry, here Ψ_{Voigt} vanishes in the low-frequency Pauli-blocked regime where no optical transitions are allowed. Here we have chosen $\Theta_0 = \pi/4$ and all other parameters are identical to those of Fig. 5.

WSM with different chemical potentials, following an approach similar to that of Ref. [65]. Qualitatively, this will lead to additional kinks in the real part of longitudinal and the imaginary part of Hall conductivity. For a noticeable quantitative difference from our calculations of the Kerr angle, the magnitude of the inversion symmetry breaking term should be large compared to the chemical potential.

Additionally, we have only considered the case of a WSM with the node separation being along the tilt axis. However, there are material examples of WSMs (LaAlGe and RAlGe, for example), in which the tilt axis can be orthogonal to the Weyl node separation. We believe that in this case, while the explicit form of the frequency-dependent σ_{xy} may change, the dc component remains intact (see discussion in Refs. [37,63]). Thus in this case also, there will be a finite contribution to the Kerr effect arising from the dc component of σ_{xy}. However, the results will be quantitatively different.

VI. SUMMARY

In this paper, we demonstrate the existence of the giant Kerr effect in tilted WSMs, which arises from the time reversal symmetry breaking in WSM thin films, and from axion electrodynamics in bulk WSM. The time reversal symmetry breaking in a WSM is captured by the Weyl node separation (Q) which explicitly determines the optical Hall conductivity ($\sigma_{xy} \propto Q$). The tilting of the Weyl nodes also plays a significant role in σ_{xy}, particularly in a type-II WSM. The existence of a finite σ_{xy} in WSMs is what leads to the giant Kerr effect

in the thin-film geometry of tilted WSMs, as long as we are away from the Pauli-blocked regime. In contrast to this, in bulk WSMs, axion electrodynamics plays an important role giving rise to optical activity and giant Kerr rotation even in the Pauli-blocked low-frequency regime ($\hbar\omega < 2\mu$ in untilted WSMs).

A key feature of our paper is the exact analytical results for the full complex optical conductivity of tilted type-I and type-II WSMs, including the impact of internode separation and finite μ. This allows us to calculate the exact polarization rotation without resorting to approximate formulas.

In the case of WSM thin films (with thickness less than wavelength of light, $d \ll \lambda$), we find that the reflection and transmission coefficients are determined completely by the optical conductivity matrix. The optical Hall conductivity is finite only for surfaces perpendicular to $\boldsymbol{Q}$, and it plays an important role in producing the giant Kerr effect when light is incident on WSM surfaces without Fermi arc states. We explicitly show that the polarization rotation in tilted WSM thin films $\Theta_{\rm Kerr} \propto \sigma_{xy}/\sigma_{xx} \propto v_F Q/\omega$. This yields the giant Kerr rotation for light incident parallel to $\boldsymbol{Q}$ with $\omega \approx 10^{14}$ rad/s or less (frequencies in the optical range and below), as long as we are not in the Pauli-blocked regime for optical transitions.

In bulk WSMs with broken time-reversal symmetry, we show that axion electrodynamics also plays an important role in the optical activity. This leads to the giant Kerr effect *even in the Pauli-blocked regime* for both type-I and type-II WSMs. The effective dielectric constant including the axion term can be expressed as $\epsilon'_{ij} = \epsilon_{ij} + \varepsilon_{ijk} Q_k \times 2i\alpha_F c/(\pi\omega)$ (see Sec. V A for details), where the second term establishes Q/ω to be the effective gyrotropy constant, analogous to magnetization in magnetic systems. The case of normal incidence on surfaces without Fermi arc states is then identical to that of Faraday geometry with light propagating parallel to the node separation. Here, we show the existence of large circular birefringence and circular dichroism, along with that of the giant Kerr effect, which is odd in Q. The case of normal incidence on surfaces with Fermi arc states turns out to be identical to that of Voigt geometry in magnetic systems. This leads to large linear birefringence and dichroism, along with a polarization angle dependent giant Kerr effect which is an even function of Q. In both cases, the axion term leads to significant optical activity and giant polarization rotation, even in the Pauli-blocked regime.

APPENDIX A: LONGITUDINAL OPTICAL CONDUCTIVITY

The Longitudinal optical conductivity can be obtained from Eq. (3), after converting the momentum sum into an integral,

$$\sigma_{ii}(\omega) = \frac{1}{8\pi^3}\int_0^{2\pi} d\phi_{\boldsymbol{k}} \int_0^{\infty} k_\perp dk_\perp \int_{-k_c}^{k_c} dk_z\, \sigma^{ii}_{\boldsymbol{k}}(\omega). \quad \text{(A1)}$$

Here we have defined the kernel

$$\sigma^{ii}_{\boldsymbol{k}}(\omega) = \frac{-in^{\rm eq}_{\boldsymbol{k}}|M_i|^2}{\hbar\omega_k}\left(\frac{1}{\omega+\omega_k+i\gamma} + \frac{1}{\omega-\omega_k+i\gamma}\right). \quad \text{(A2)}$$

The equilibrium population inversion (at $T = 0$) is given by $n^{\rm eq}_{\boldsymbol{k}} = \Theta(\mu - \hbar v_f k - \hbar\xi v_t k_z^\xi) - \Theta(\mu + \hbar v_f k - \hbar\xi v_t k_z^\xi)$ and $\hbar\omega_k = 2\hbar v_F k$ is the energy difference between the conduction and the valance band, which is independent of the tilt velocity. Here $k = \sqrt{k_\perp^2 + (k_z^\xi)^2}$. The real and the imaginary parts can be separated in the limit $\gamma \to 0$, using the Dirac identity

$$\lim_{\epsilon\to 0}\frac{1}{x+i\epsilon} = \mathcal{P}\int_{-\infty}^{\infty}\left(\frac{1}{x}\right) - i\pi\delta(x). \quad \text{(A3)}$$

Here $\mathcal{P}$ denotes the principal value. We find that the longitudinal optical conductivity of the time reversal symmetry broken Weyl semimetal is the sum of the optical conductivities of the two Weyl nodes. Thus we just calculate the conductivity of the $\xi = 1$ node and multiply it by two. This allows us to substitute $k_z^\xi \to k_z$ and $\xi v_t \to v_t$ in the expressions below.

1. Re$[\sigma_{xx}(\omega)]$

Thus, the real part of longitudinal optical conductivity is given by

$$\mathrm{Re}[\sigma_{ii}] = -\frac{1}{(2\pi)^3}\int_0^{2\pi} d\phi_{\boldsymbol{k}} \int_0^{\infty} k_\perp dk_\perp \int_{-k_c}^{k_c} dk_z \times \frac{n^{\rm eq}_{\boldsymbol{k}}}{\hbar\omega_{\boldsymbol{k}}}|M_i|^2\pi\delta(\omega-\omega_{\boldsymbol{k}}). \quad \text{(A4)}$$

Here, only the optical matrix is dependent on $\phi_{\boldsymbol{k}}$, and the angular integration leads to

$$\int_0^{2\pi}|M_x|^2 d\phi_{\boldsymbol{k}} = \pi e^2 v_F^2\left(1+\frac{k_z^2}{k^2}\right). \quad \text{(A5)}$$

Thus we obtain

$$\mathrm{Re}[\sigma_{xx}(\omega)] = \frac{e^2 v_F^2}{8\pi}\int_0^{\infty} k_\perp dk_\perp \int_{-k_c}^{k_c}\left(1+\frac{k_z^2}{k^2}\right)dk_z \times \frac{\delta(\omega-\omega_{\boldsymbol{k}})}{\hbar v_F k}[\Theta(\mu-\hbar v_F k-\hbar|v_t|k_z) - \Theta(\mu+\hbar v_F k-\hbar|v_t|k_z)]. \quad \text{(A6)}$$

Now, the integration for $k_\perp$ can easily be carried using the roots (x_i) of the argument in the Dirac delta function:

$$\delta(f(x)) = \sum_{x_i}\frac{\delta(x-x_i)}{|f'(x_i)|}. \quad \text{(A7)}$$

Substituting the roots in the delta function leads to a much simpler one-dimensional integral,

$$\mathrm{Re}[\sigma_{xx}(\omega)] = \frac{e^2}{16\pi\hbar}\int_{-\omega/2v_F}^{\omega/2v_F} dk_z\left[\left(\frac{2v_F k_z}{\omega}\right)^2+1\right] \times [\Theta(\mu-\hbar v_t k_z+\hbar\omega/2) - \Theta(\mu-\hbar v_t k_z-\hbar\omega/2)]. \quad \text{(A8)}$$

Equation (A8) can be expressed in a dimensionless form:

$$\mathrm{Re}[\sigma_{xx}(\omega)] = \sigma_\omega F_{xx}, \quad \text{where} \quad \sigma_\omega \equiv \frac{e^2}{6h}\frac{\omega}{v_F}, \quad \text{(A9)}$$

and

$$F_{xx} = \frac{3}{8}\int_{-1}^{1} dx(1+x^2)(\Theta_+ - \Theta_-), \quad \text{(A10)}$$

where we have defined $\Theta_\pm = \Theta[\frac{2\mu}{\hbar\omega} - \alpha_t x \pm 1]$, and $x = 2v_F k_z/\omega$. Evaluating the integral in Eq. (A10) for the two cases of $|\alpha_t| < 1$ and $|\alpha_t| > 1$ leads to Eq. (7) and Eq. (9) of the main text, respectively.

2. Re[$\sigma_{zz}(\omega)$]

Following the same procedure as above, the angular integration leads to

$$\int_0^{2\pi} |M_z|^2 d\phi_k = 2\pi e^2 v_F^2 \frac{k_\perp^2}{k^2}. \tag{A11}$$

Thus the longitudinal optical conductivity in this case is given by

$$\mathrm{Re}[\sigma_{zz}] = \frac{e^2 v_F^2}{4\pi} \int_0^\infty k_\perp dk_\perp \int_{-k_c}^{k_c} \frac{k_\perp^2 dk_z}{k_\perp^2 + k_z^2} \frac{\delta(\omega - \omega_k)}{\hbar v_F k} \times [\Theta(\mu - \hbar v_F k - \hbar v_t k_z) - \Theta(\mu + \hbar v_F k - \hbar v_t k_z)]. \tag{A12}$$

Performing the $k_\perp$ integral using the roots of the δ function, we have

$$\mathrm{Re}[\sigma_{zz}(\omega)] = \frac{e^2}{8\pi\hbar} \int_{-\omega/2v_F}^{\omega/2v_F} dk_z \left[\left(1 - \frac{2v_F k_z}{\omega}\right)^2\right] \times [\Theta(\mu - \hbar|v_t|k_z + \hbar\omega/2) - \Theta(\mu - \hbar|v_t|k_z - \hbar\omega/2)]. \tag{A13}$$

Equation (A13) can be expressed in a dimensionless form as

$$\mathrm{Re}[\sigma_{zz}(\omega)] = 2\,\sigma_\omega F_{zz}, \tag{A14}$$

where we have defined

$$F_{zz} = \frac{3}{8} \int_{-1}^{1} dx(1 - x^2)(\Theta_+ - \Theta_-) \tag{A15}$$

and $\Theta_\pm$ are defined below Eq. (A10). Performing the integral in Eq. (A15) for the two cases of $|\alpha_t| < 1$ and $|\alpha_t| > 1$ leads to Eq. (17) and Eq. (19), respectively.

3. Im[$\sigma_{xx}(\omega)$] and Im[$\sigma_{zz}(\omega)$]

Once the real parts are obtained and they converge to a constant as $\omega \to \infty$, the imaginary parts are computed using the Kramers-Kronig relation for the imaginary part of the optical conductivity,

$$\mathrm{Im}[\sigma_{ii}(\omega)] = \frac{-2\omega}{\pi} \int_0^{\omega_c} \frac{\mathrm{Re}[\sigma_{xx}(\omega') - \sigma_{xx}(0)]}{\omega'^2 - \omega^2} d\omega'. \tag{A16}$$

Note that since the low-energy Weyl Hamiltonian has an infinite bandwidth, with an infinite filled sea of quasiparticles even in the ground state, we are forced to use an upper frequency cutoff ($\hbar\omega_c = \hbar v_F k_c$) for the integral. This cutoff was not needed in the calculation of the real part of the longitudinal conductivity due to the presence of the delta function.

APPENDIX B: TRANSVERSE OPTICAL CONDUCTIVITY

The transverse optical Hall conductivity is given by

$$\sigma_{ij}(\omega) = \frac{1}{8\pi^3} \int_0^{2\pi} d\phi_k \int_0^\infty k_\perp dk_\perp \int_{-k_c}^{k_c} dk_z\, \sigma_k^{ij}(\omega), \tag{B1}$$

where the conductivity kernel is given by

$$\sigma_k^{ij} = \frac{-i n_k^{\mathrm{eq}}}{\hbar\omega_k} \left(\frac{M_j M_i^*}{\omega + \omega_k + i\gamma} + \frac{M_j^* M_i}{\omega - \omega_k + i\gamma}\right). \tag{B2}$$

Writing in terms of real and imaginary parts of M^{vc}, we have

$$\sigma_{xy} = \int \frac{d^3k}{8\pi^3} \frac{n_k^{\mathrm{eq}}}{\hbar\omega_k} \left(M_R^x M_I^y - M_I^x M_R^y\right) \times \left(\frac{1}{\omega^+ + \omega_k} - \frac{1}{\omega^+ - \omega_k}\right). \tag{B3}$$

Here $\omega^+ = \omega + i\gamma$. As in the previous cases, performing the angular integral over the ϕ_k-dependent optical matrix elements yields

$$\int_0^{2\pi} \left(M_R^x M_I^y - M_I^x M_R^y\right) d\phi_k = \frac{2\pi\xi k_z^\xi}{k}. \tag{B4}$$

Again, the real and imaginary parts can now be evaluated separately in the limit $\gamma \to 0$ using the Dirac identity. Before proceeding, we note that Eq. (B3) differs in form from Eq. (A5) by a factor of i. As a consequence now δ functions appear in Im[$\sigma_{xy}(\omega)$]. In contrast to the longitudinal conductivity, for the transverse case, the two nodes have to be treated together and the internode separation becomes important.

1. Im[σ_{xy}]

Using the Dirac identity in Eq. (A3), the imaginary part of $\sigma_{xy}(\omega)$ can be expressed as

$$\mathrm{Im}[\sigma_{xy}] = \frac{e^2 v_F^2}{4\pi} \sum_{\xi=\pm1} \xi \int k_\perp dk_\perp dk_z^\xi \frac{k_z^\xi}{k} \frac{n_k^{\mathrm{eq}}}{\hbar\omega_k} \delta(\omega - \omega_k). \tag{B5}$$

Performing the $k_\perp$ integral and using the δ function lead to the following one-dimensional integral,

$$\mathrm{Im}[\sigma_{\mathrm{xy}}(\omega)] = \frac{e^2 v_F}{8\pi\hbar\omega} \sum_{\xi=\pm1} \xi \int_{-\omega/2v_F}^{\omega/2v_F} k_z^\xi dk_z^\xi \times \left[\Theta\left(1 - \frac{\hbar\omega}{2\mu} - \frac{\hbar\xi v_t k_z^\xi}{\mu}\right) - \Theta\left(1 + \frac{\hbar\omega}{2\mu} - \frac{\hbar\xi v_t k_z^\xi}{\mu}\right)\right]. \tag{B6}$$

Equation (B6) can be expressed as

$$\mathrm{Im}[\sigma_{xy}(\omega)] = \frac{3\sigma_\omega}{2} \frac{\mu^2}{\hbar^2\omega^2} F_{xy}, \tag{B7}$$

where we have defined

$$F_{xy} = \sum_{\xi=\pm1} \xi \int_{-\frac{\hbar\omega}{2\mu}}^{\frac{\hbar\omega}{2\mu}} x dx \sum_{p=\pm} \Theta\left(1 - \xi\alpha_t x - p\frac{\hbar\omega}{2\mu}\right). \tag{B8}$$

Solving Eq. (B8) leads to Eq. (25) [Eq. (27)] for the cases of $|\alpha_t| < 1$ ($|\alpha_t| > 1$).

2. Re[σ_{xy}]

Having obtained the imaginary part of the transverse conductivity, its real part can be obtained from the Kramers-Kronig relation for conductivity,

$$\mathrm{Re}[\sigma_{ij}(\omega) - \sigma_{ij}(0)] = \frac{2\omega^2}{\pi}\int_0^{\omega_c} d\omega' \frac{\mathrm{Im}[\sigma_{ij}(\omega')]}{\omega'[\omega'^2 - \omega^2]}. \quad \text{(B9)}$$

Here the use of an upper frequency cutoff is forced to cut off the contribution from the infinite filled Fermi sea in the low-energy model of Weyl (or Dirac) semimetals. The ac (finite ω) component of the real part of the transverse conductivity calculated from Eq. (B9) for type-I and type-II WSMs is presented in Eq. (30) and Eq. (31), respectively.

It turns out that the dc component of the transverse conductivity in a WSM is finite, and it has to be calculated separately as Eq. (B9) only gives the finite-frequency contributions. The dc component (real part) of the transverse conductivity is given by

$$\mathrm{Re}\big[\sigma_{xy}^{dc}\big] = \frac{e^2 v_F}{4\pi^2}\sum_{\xi=\pm1}\int_0^{\infty} k_\perp dk_\perp \int_{-k_c}^{k_c}\left(\frac{n_{\boldsymbol{k}}^{\mathrm{eq}}}{\hbar\omega_k}\right)\frac{\xi k_z^\xi}{k^2}dk_z^\xi, \quad \text{(B10)}$$

where $\xi k_z^\xi/k$ results from the optical matrix element, and $1/k$ from $1/\omega_k$. Further change of variable from $k_z^\xi \to k_z$ leads to

$$\mathrm{Re}\big[\sigma_{xy}^{dc}\big] = \frac{e^2}{4\pi h}\sum_{\xi=\pm1}\int_0^{\infty} k_\perp dk_\perp \int_{-k_c-\xi Q}^{k_c-\xi Q}\frac{\xi n_{\boldsymbol{k}}^{\mathrm{eq}} k_z dk_z}{\left(k_\perp^2 + k_z^2\right)^{3/2}}. \quad \text{(B11)}$$

It turns out that Eq. (B11) has an *intrinsic* contribution (finite for $\mu \to 0$) and an *extrinsic* contribution (which vanishes in the $\mu \to 0$ limit). To evaluate them it is useful to express the population inversion as a sum of extrinsic (in square brackets) and intrinsic contributions (independent of μ), $n_{\boldsymbol{k}}^{\mathrm{eq}} = [\Theta(\mu - \hbar v_F k_\xi - \hbar\xi v_t k_z^\xi) - \Theta(\mu + \hbar v_F k_\xi - \hbar\xi v_t k_z^\xi) + 1] - 1$. Evaluating these two terms separately, we obtain the intrinsic contribution $\propto \sigma_Q$ and the extrinsic contribution $\propto \sigma_\mu$. Their explicit expressions for the two cases of $|\alpha_t| < 1$ and $|\alpha_t| > 1$ are presented in Eq. (28) and Eq. (29), respectively.

APPENDIX C: AXION ELECTRODYNAMICS

The Maxwell equations inside the bulk of a material are modified by the presence of an axionic term. This modification is derived by adding the additional topological magnetoelectric term in the Lagrangian [54], $\delta\mathcal{L} = \alpha_F c\epsilon_0 \vartheta \boldsymbol{E}\cdot\boldsymbol{B}/\pi$, with α_F being the fine-structure constant, and ϑ is the axion field. One experimentally demonstrated manifestation of this axionic term in materials is the topological magnetoelectric effect. Its impact on the material properties is primarily based on additional topological contributions to the electric polarization and magnetization [54],

$$\boldsymbol{D} = \boldsymbol{\epsilon}\boldsymbol{E} + c\epsilon_0\alpha_F\vartheta\boldsymbol{B}/\pi, \quad \text{(C1)}$$

$$\boldsymbol{H} = \boldsymbol{B}/\mu_p - c\epsilon_0\alpha_F\vartheta\boldsymbol{E}/\pi, \quad \text{(C2)}$$

where $\boldsymbol{\epsilon}$ is the dielectric tensor, and μ_p is the permeability. The Maxwell field equations with sources are thus modified as

$$\nabla\cdot(\boldsymbol{\epsilon}\boldsymbol{E} + c\epsilon_0\alpha_F\vartheta\boldsymbol{B}/\pi) = \rho \Rightarrow \nabla\cdot(\boldsymbol{\epsilon}\boldsymbol{E}) = (\rho + \rho_\vartheta), \quad \text{(C3)}$$

where $\rho_\vartheta = -c\epsilon_0\alpha_F\nabla\vartheta\cdot\boldsymbol{B}/(\pi)$ is the axion charge density. From Eq. (43), we have

$$\nabla\times(\boldsymbol{B}/\mu_p - c\epsilon_0\alpha_F\vartheta\boldsymbol{E}/\pi) = \boldsymbol{J} + \frac{\partial}{\partial t}(\boldsymbol{\epsilon}\boldsymbol{E} + c\epsilon_0\alpha_F\vartheta\boldsymbol{B}/\pi)$$
$$\Rightarrow \nabla\times\boldsymbol{B} = \mu_p\boldsymbol{J} + \boldsymbol{\epsilon}\mu_p\frac{\partial\boldsymbol{E}}{\partial t} + \boldsymbol{J}_\vartheta. \quad \text{(C4)}$$

Here, $\boldsymbol{J}_\vartheta = \alpha_F c\epsilon_0\mu_p(\dot\vartheta\boldsymbol{B} + \nabla\vartheta\times\boldsymbol{E})/\pi$ is the axion field dependent current density. The other two sourceless Maxwell equations remain unchanged as

$$\nabla\cdot\boldsymbol{B} = 0, \quad \text{(C5)}$$

$$\nabla\times\boldsymbol{E} + \partial_t\boldsymbol{B} = 0. \quad \text{(C6)}$$

In a WSM, the axion field can be expressed in terms of internodal separation in the momentum ($\boldsymbol{Q}$) and energy ($\mathcal{Q}_0$) space, $\vartheta(\boldsymbol{r}, t) = 2\boldsymbol{Q}\cdot\boldsymbol{r} - 2\mathcal{Q}_0 t$. For a WSM which preserves the inversion symmetry, we have $\mathcal{Q}_0 = 0$, and thus $\nabla\vartheta = \boldsymbol{Q}$ and $\dot\vartheta = 0$. Now eliminating **B** from Eq. (C4) using the other modified Maxwell equations and using $\boldsymbol{J} = \boldsymbol{\sigma}\cdot\boldsymbol{E}$, we obtain the wave propagation equation in a time reversal symmetry broken WSM,

$$\nabla(\nabla\cdot\boldsymbol{E}) - \nabla^2\boldsymbol{E} = -\mu_p\boldsymbol{\sigma}\frac{\partial\boldsymbol{E}}{\partial t} - \boldsymbol{\epsilon}\mu_p\frac{\partial^2\boldsymbol{E}}{\partial t^2}$$
$$- \frac{2\alpha_F c\epsilon_0\mu_p}{\pi}\boldsymbol{Q}\times\frac{\partial\boldsymbol{E}}{\partial t}. \quad \text{(C7)}$$

Using Eq. (C7), we now explore the wave propagation in the two geometries with $\boldsymbol{n} \parallel \boldsymbol{Q}$ (Faraday geometry) and $\boldsymbol{n} \perp \boldsymbol{Q}$ (Voigt geometry) in the next two subsections.

1. The Faraday geometry

For an electric field $\mathbf{E} = E_o e^{i(\boldsymbol{k}\cdot\boldsymbol{r} - \omega t)}$, with amplitude E_o, propagating in the $\hat z$ direction ($\boldsymbol{k} = k\hat z$), the left-hand side of Eq. (44) yields

$$\begin{pmatrix}\partial^2/\partial z^2 & 0 & 0\\ 0 & \partial^2/\partial z^2 & 0\\ 0 & 0 & 0\end{pmatrix}\mathbf{E} = -k^2\mathbf{E}. \quad \text{(C8)}$$

The right-hand side of Eq. (44) results in

$$-\epsilon_{ij}\frac{\omega^2}{c^2}\boldsymbol{E} - \frac{2i\omega\alpha_F\boldsymbol{Q}\cdot\boldsymbol{E}}{c\pi}, \quad \text{(C9)}$$

where $\epsilon_{ij} = \epsilon_b\delta_{ij} + \frac{i\sigma}{\epsilon_0\omega}$. Substituting $k = n\omega/c$, the wave equation becomes

$$n^2\begin{pmatrix}E_x\\E_y\\0\end{pmatrix} = \frac{i}{\omega\epsilon_0}\begin{pmatrix}\sigma_{xx} & \sigma_{xy} & 0\\ -\sigma_{xy} & \sigma_{yy} & 0\\ 0 & 0 & \sigma_{zz}\end{pmatrix}\begin{pmatrix}E_x\\E_y\\E_z\end{pmatrix}$$
$$+\begin{pmatrix}0 & \frac{2i\alpha_F Qc}{\pi\omega} & 0\\ -\frac{2i\alpha_F Qc}{\pi\omega} & 0 & 0\\ 0 & 0 & 0\end{pmatrix}\begin{pmatrix}E_x\\E_y\\E_z\end{pmatrix} + \epsilon_b\mathbb{I}\begin{pmatrix}E_x\\E_y\\E_z\end{pmatrix}. \quad \text{(C10)}$$

Here $\mathbb{I}$ denotes the identity matrix. Thus, the effective dielectric tensor inside the WSM becomes

$$n^2\begin{pmatrix}E_x\\E_y\\0\end{pmatrix}=\begin{pmatrix}\epsilon'_{xx}&\epsilon'_{xy}&0\\-\epsilon'_{xy}&\epsilon'_{yy}&0\\0&0&\epsilon'_{zz}\end{pmatrix}\begin{pmatrix}E_x\\E_y\\E_z\end{pmatrix}, \tag{C11}$$

where the diagonal components are given by

$$\epsilon'_{xx}(\epsilon'_{zz})=\epsilon_b+\frac{i}{\omega\epsilon_0}\sigma_{xx}(\sigma_{zz}) \tag{C12}$$

and the off-diagonal elements responsible for optical activity are given by

$$\epsilon'_{xy}=\frac{2i}{\omega}\left(\frac{\alpha_F Qc}{\pi}+\frac{\sigma_{xy}}{\epsilon_0}\right). \tag{C13}$$

2. The Voigt geometry

In this case, the electric field propagates in the $\hat{x}$ direction ($\boldsymbol{k}=k\hat{x}$).

Since the right-hand side of the wave equation contains only time derivatives, the terms on the right-hand side remain unchanged and are given by Eq. (C9) in this geometry too.

The left-hand side of the wave equation containing spatial derivatives is modified for this geometry as

$$\begin{pmatrix}0&0&0\\0&\partial^2/\partial x^2&0\\0&0&\partial^2/\partial x^2\end{pmatrix}\mathbf{E}=-k^2\mathbf{E} \tag{C14}$$

with the second term $\nabla(\nabla\cdot\boldsymbol{E})=0$ in this case too. For this geometry, Eqs. (C10) and (C11) are modified to be

$$n^2\begin{pmatrix}0\\E_y\\E_z\end{pmatrix}=\frac{i}{\omega\epsilon_0}\begin{pmatrix}\sigma_{xx}&\sigma_{xy}&0\\-\sigma_{xy}&\sigma_{yy}&0\\0&0&\sigma_{zz}\end{pmatrix}\begin{pmatrix}E_x\\E_y\\E_z\end{pmatrix}+\begin{pmatrix}0&\frac{2i\alpha_F Qc}{\pi\omega}&0\\-\frac{2i\alpha_F Qc}{\pi\omega}&0&0\\0&0&0\end{pmatrix}\begin{pmatrix}E_x\\E_y\\E_z\end{pmatrix}+\epsilon_b\mathbb{I}\begin{pmatrix}E_x\\E_y\\E_z\end{pmatrix}, \tag{C15}$$

$$n^2\begin{pmatrix}0\\E_y\\E_z\end{pmatrix}=\begin{pmatrix}\epsilon'_{xx}&\epsilon'_{xy}&0\\-\epsilon'_{xy}&\epsilon'_{yy}&0\\0&0&\epsilon'_{zz}\end{pmatrix}\begin{pmatrix}E_x\\E_y\\E_z\end{pmatrix}. \tag{C16}$$

Here, the elements of the modified dielectric tensor are given by Eqs. (C12) and (C13).

[1] H. B. Nielsen and M. Ninomiya, The Adler-Bell-Jackiw anomaly and Weyl fermions in a crystal, Phys. Lett. B **130**, 389 (1983).

[2] X. Wan, A. M. Turner, A. Vishwanath, and S. Y. Savrasov, Topological semimetal and Fermi-arc surface states in the electronic structure of pyrochlore iridates, Phys. Rev. B **83**, 205101 (2011).

[3] A. A. Soluyanov, D. Gresch, Z. Wang, Q. Wu, M. Troyer, X. Dai, and B. B. Andrei, Type-II Weyl semimetals, Nature (London) **527**, 495 (2015).

[4] S. Jia, Xu Su-Yang, and H. M. Zahid, Weyl semimetals, Fermi arcs and chiral anomalies, Nat. Mater. **15**, 1140 (2016).

[5] A. Bansil, H. Lin, and T. Das, Colloquium: Topological band theory, Rev. Mod. Phys. **88**, 021004 (2016).

[6] B. Yan and C. Felser, Topological materials: Weyl semimetals, Annu. Rev. Condens. Matter Phys. **8**, 337 (2017).

[7] N. P. Armitage, E. J. Mele, and A. Vishwanath, Weyl and Dirac semimetals in three-dimensional solids, Rev. Mod. Phys. **90**, 015001 (2018).

[8] A. A. Burkov and L. Balents, Weyl Semimetal in a Topological Insulator Multilayer, Phys. Rev. Lett. **107**, 127205 (2011).

[9] A. Juyal, A. Agarwal, and S. Mukhopadhyay, Negative Longitudinal Magnetoresistance in the Density Wave Phase of $Y_2Ir_2O_7$, Phys. Rev. Lett. **120**, 096801 (2018).

[10] C. Wang, Y. Zhang, J. Huang, S. Nie, G. Liu, A. Liang, Y. Zhang, B. Shen, J. Liu, C. Hu, Y. Ding, D. Liu, Y. Hu, S. He, L. Zhao, L. Yu, J. Hu, J. Wei, Z. Mao, Y. Shi, X. Jia, F. Zhang, S. Zhang, F. Yang, Z. Wang, Q. Peng, H. Weng, X. Dai, Z. Fang, Z. Xu, C. Chen, and X. J. Zhou, Observation of Fermi arc and its connection with bulk states in the candidate type-II Weyl semimetal WTe_2, Phys. Rev. B **94**, 241119(R) (2016).

[11] P. Li, Y. Wen, X. He, Q. Zhang, C. Xia, Z.-M. Yu, S. A. Yang, Z. Zhu, H. N. Alshareef, and X.-X. Zhang, Evidence for topological type-II Weyl semimetal WTe_2, Nat. Commun. **8**, 2150 (2017).

[12] Y. Sun, S.-C. Wu, M. N. Ali, C. Felser, and B. Yan, Prediction of Weyl semimetal in orthorhombic $MoTe_2$, Phys. Rev. B **92**, 161107(R) (2015).

[13] K. Deng, G. Wan, P. Deng, K. Zhang, S. Ding, E. Wang, M. Yan, H. Huang, H. Zhang, Z. Xu, J. Denlinger, A. Fedorov, H. Yang, W. Duan, H. Yao, Y. Wu, S. Fan, H. Zhang, X. Chen, and S. Zhou, Experimental observation of topological Fermi arcs in type-II Weyl semimetal $MoTe_2$, Nat. Phys. **12**, 1105 (2016).

[14] L. Huang, T. M. McCormick, M. Ochi, Z. Zhao, M.-T. Suzuki, R. Arita, Y. Wu, D. Mou, H. Cao, J. Yan, N. Trivedi, and A. Kaminski, Spectroscopic evidence for a type II Weyl semimetallic state in $MoTe_2$, Nat. Mater. **15**, 1155 (2016).

[15] Z. Wang, D. Gresch, A. A. Soluyanov, W. Xie, S. Kushwaha, X. Dai, M. Troyer, R. J. Cava, and B. A. Bernevig, $MoTe_2$: A Type-II Weyl Topological Metal, Phys. Rev. Lett. **117**, 056805 (2016).

[16] A. Tamai, Q. S. Wu, I. Cucchi, F. Y. Bruno, S. Riccò, T. K. Kim, M. Hoesch, C. Barreteau, E. Giannini, C. Besnard, A. A. Soluyanov, and F. Baumberger, Fermi Arcs and Their Topological Character in the Candidate Type-II Weyl Semimetal $MoTe_2$, Phys. Rev. X **6**, 031021 (2016).

[17] J. Jiang, Z. K. Liu, Y. Sun, H. F. Yang, C. R. Rajamathi, Y. P. Qi, L. X. Yang, C. Chen, H. Peng, C.-C. Hwang, S. Z. Sun, S.-K. Mo, I. Vobornik, J. Fujii, S. S. P. Parkin, C. Felser, B. H. Yan, and Y. L. Chen, Signature of type-II Weyl semimetal phase in $MoTe_2$, Nat. Commun. **8**, 13973 (2017).

[18] I. Belopolski, S.-Y. Xu, Y. Ishida, X. Pan, P. Yu, D. S. Sanchez, H. Zheng, M. Neupane, N. Alidoust, G. Chang, T.-R. Chang, Y. Wu, G. Bian, S.-M. Huang, C.-C. Lee, D. Mou, L. Huang, Y. Song, B. Wang, G. Wang, Y.-W. Yeh, N. Yao, J. E. Rault, P. Le Févre, F. Bertran, H.-T. Jeng, T. Kondo, A. Kaminski, H. Lin,

Z. Liu, F. Song, S. Shin, and M. Z. Hasan, Fermi arc electronic structure and Chern numbers in the type-II Weyl semimetal candidate $Mo_xW_{1-x}Te_2$, Phys. Rev. B **94**, 085127 (2016).

[19] T.-R. Chang, S.-Y. Xu, G. Chang, C.-C. Lee, S.-M. Huang, B. Wang, G. Bian, H. Zheng, D. S. Sanchez, I. Belopolski, N. Alidoust, M. Neupane, A. Bansil, H.-T. Jeng, H. Lin, and H. M. Zahid, Prediction of an arc-tunable Weyl fermion metallic state in $Mo_xW_{1-x}Te_2$, Nat. Commun. **7**, 10639 (2016).

[20] S.-Y. Xu, I. Belopolski, N. Alidoust, M. Neupane, G. Bian, C. Zhang, R. Sankar, G. Chang, Z. Yuan, C.-C. Lee, S.-M. Huang, H. Zheng, J. Ma, D. S. Sanchez, B. Wang, A. Bansil, F. Chou, P. P. Shibayev, H. Lin, S. Jia, and M. Z. Hasan, Discovery of a Weyl fermion semimetal and topological Fermi arcs, Science **349**, 613 (2015).

[21] B. Q. Lv, H. M. Weng, B. B. Fu, X. P. Wang, H. Miao, J. Ma, P. Richard, X. C. Huang, L. X. Zhao, G. F. Chen, Z. Fang, X. Dai, T. Qian, and H. Ding, Experimental discovery of Weyl semimetal TaAs, Phys. Rev. X **5**, 031013 (2015).

[22] B. Q. Lv, N. Xu, H. M. Weng, J. Z. Ma, P. Richard, X. C. Huang, L. X. Zhao, G. F. Chen, C. E. Matt, F. Bisti, V. N. Strocov, J. Mesot, Z. Fang, X. Dai, T. Qian, M. Shi, and H. Ding, Observation of Weyl nodes in TaAs, Nat. Phys. **11**, 724 (2015).

[23] L. X. Yang, Z. K. Liu, Y. Sun, H. Peng, H. F. Yang, T. Zhang, B. Zhou, Y. Zhang, Y. F. Guo, M. Rahn, D. Prabhakaran, Z. Hussain, S.-K. Mo, C. Felser, B. Yan, and Y. L. Chen, Weyl semimetal phase in the non-centrosymmetric compound TaAs, Nat. Phys. **11**, 728 (2015).

[24] N. Xu, H. M. Weng, B. Q. Lv, C. E. Matt, J. Park, F. Bisti, V. N. Strocov, D. Gawryluk, E. Pomjakushina, K. Conder, N. C. Plumb, M. Radovic, G. Autés, O. V. Yazyev, Z. Fang, X. Dai, T. Qian, J. Mesot, H. Ding, and M. Shi, Observation of Weyl nodes and Fermi arcs in tantalum phosphide, Nat. Commun. **7**, 11006 (2016).

[25] S.-Y. Xu, I. Belopolski, D. S. Sanchez, C. Zhang, G. Chang, C. Guo, G. Bian, Z. Yuan, H. Lu, T.-R. Chang, P. P. Shibayev, M. L. Prokopovych, N. Alidoust, H. Zheng, C.-C. Lee, S.-M. Huang, R. Sankar, F. Chou, C.-H. Hsu, H.-T. Jeng, A. Bansil, T. Neupert, V. N. Strocov, H. Lin, S. Jia, and M. Z. Hasan, Experimental discovery of a topological Weyl semimetal state in TaP, Sci. Adv. **1**, e1501092 (2015).

[26] Y. Sun, S.-C. Wu, and B. Yan, Topological surface states and Fermi arcs of the noncentrosymmetric Weyl semimetals TaAs, TaP, NbAs, and NbP, Phys. Rev. B **92**, 115428 (2015).

[27] E. Haubold, K. Koepernik, D. Efremov, S. Khim, A. Fedorov, Y. Kushnirenko, J. van den Brink, S. Wurmehl, B. Büchner, T. K. Kim, M. Hoesch, K. Sumida, K. Taguchi, T. Yoshikawa, A. Kimura, T. Okuda, and S. V. Borisenko, Experimental realization of type-II Weyl state in noncentrosymmetric $TaIrTe_4$, Phys. Rev. B **95**, 241108(R) (2017).

[28] S.-Y. Xu, N. Alidoust, G. Chang, H. Lu, B. Singh, I. Belopolski, D. S. Sanchez, X. Zhang, G. Bian, H. Zheng, M.-A. Husanu, Y. Bian, S.-M. Huang, C.-H. Hsu, T.-R. Chang, H.-T. Jeng, A. Bansil, T. Neupert, V. N. Strocov, H. Lin, S. Jia, and M. Z. Hasan, Discovery of Lorentz-violating type II Weyl fermions in LaAlGe, Sci. Adv. **3**, e1603266 (2017).

[29] Y. Ferreiros, A. A. Zyuzin, and J. H. Bardarson, Anomalous Nernst and thermal Hall effects in tilted Weyl semimetals, Phys. Rev. B **96**, 115202 (2017).

[30] P. Hosur, S. A. Parameswaran, and A. Vishwanath, Charge Transport in Weyl Semimetals, Phys. Rev. Lett. **108**, 046602 (2012).

[31] S. Wang, B.-C. Lin, A.-Q. Wang, D.-P. Yu, and Z.-M. Liao, Quantum transport in Dirac and Weyl semimetals: A review, Adv. Phys.: X **2**, 518 (2017).

[32] K. Das and A. Agarwal, Linear magnetochiral transport in tilted type-I and type-II Weyl semimetals, Phys. Rev. B **99**, 085405 (2019).

[33] A. A. Zyuzin and A. A. Burkov, Topological response in Weyl semimetals and the chiral anomaly, Phys. Rev. B **86**, 115133 (2012).

[34] D. T. Son and N. Yamamoto, Berry Curvature, Triangle Anomalies, and the Chiral Magnetic Effect in Fermi Liquids, Phys. Rev. Lett. **109**, 181602 (2012).

[35] A. A. Burkov, Anomalous Hall Effect in Weyl Metals, Phys. Rev. Lett. **113**, 187202 (2014).

[36] K.-S. Kim, H.-J. Kim, and M. Sasaki, Boltzmann equation approach to anomalous transport in a Weyl metal, Phys. Rev. B **89**, 195137 (2014).

[37] J. F. Steiner, A. V. Andreev, and D. A. Pesin, Anomalous Hall Effect in Type-I Weyl Metals, Phys. Rev. Lett. **119**, 036601 (2017).

[38] S. Zhong, J. Orenstein, and J. E. Moore, Optical Gyrotropy from Axion Electrodynamics in Momentum Space, Phys. Rev. Lett. **115**, 117403 (2015).

[39] P. Goswami, G. Sharma, and S. Tewari, Optical activity as a test for dynamic chiral magnetic effect of Weyl semimetals, Phys. Rev. B **92**, 161110(R) (2015).

[40] M. Trescher, B. Sbierski, P. W. Brouwer, and E. J. Bergholtz, Quantum transport in Dirac materials: Signatures of tilted and anisotropic Dirac and Weyl cones, Phys. Rev. B **91**, 115135 (2015).

[41] P. Hosur and X.-L. Qi, Tunable circular dichroism due to the chiral anomaly in Weyl semimetals, Phys. Rev. B **91**, 081106(R) (2015).

[42] A. A. Burkov, Giant planar Hall effect in topological metals, Phys. Rev. B **96**, 041110(R) (2017).

[43] A. Thakur, K. Sadhukhan, and A. Agarwal, Dynamic current-current susceptibility in three-dimensional Dirac and Weyl semimetals, Phys. Rev. B **97**, 035403 (2018).

[44] L. Wu, S. Patankar, T. Morimoto, N. L. Nair, E. Thewalt, A. Little, J. G. Analytis, J. E. Moore, and J. Orenstein, Giant anisotropic nonlinear optical response in transition metal monopnictide Weyl semimetals, Nat. Phys. **13**, 350 (2016).

[45] Q. Ma, S.-Y. Xu, C.-K. Chan, C.-L. Zhang, G. Chang, Y. Lin, W. Xie, T. Palacios, H. Lin, S. Jia, P. A. Lee, P. Jarillo-Herrero, and N. Gedik, Direct optical detection of Weyl fermion chirality in a topological semimetal, Nat. Phys. **13**, 842 (2017).

[46] E. Barnes, J. J. Heremans, and D. Minic, Electromagnetic Signatures of the Chiral Anomaly in Weyl Semimetals, Phys. Rev. Lett. **117**, 217204 (2016).

[47] K. Mehdi, R. Mohit, and T. Nandini, Theory of Kerr and Faraday rotations and linear dichroism in topological Weyl semimetals, Sci. Rep. **5**, 12683 (2015).

[48] J. Yang, J. Kim, and K.-S. Kim, Transmission and reflection coefficients and Faraday/Kerr rotations as a function of applied magnetic fields in spin-orbit coupled Dirac metals, Phys. Rev. B **98**, 075203 (2018).

[49] S. Chen, C. Mi, W. Wu, W. Zhang, W. Shu, H. Luo, and S. Wen, Weak-value amplification for Weyl-point separation in momentum space, New J. Phys. **20**, 103050 (2018).

[50] K. Halterman, M. Alidoust, and A. Zyuzin, Epsilon-near-zero response and tunable perfect absorption in Weyl semimetals, Phys. Rev. B **98**, 085109 (2018).

[51] O. V. Kotov and Yu. E. Lozovik, Dielectric response and novel electromagnetic modes in three-dimensional Dirac semimetal films, Phys. Rev. B **93**, 235417 (2016).

[52] A. Singh and J. P. Carbotte, Effect of chiral anomaly on the circular dichroism and Hall angle in doped and tilted Weyl semimetals, Phys. Rev. B **99**, 235134 (2019).

[53] K. Das and A. Agarwal, Berry curvature induced thermopower in type-I and type-II Weyl semimetals, Phys. Rev. B **100**, 085406 (2019).

[54] F. Wilczek, Two Applications of Axion Electrodynamics, Phys. Rev. Lett. **58**, 1799 (1987).

[55] L. Wu, M. Salehi, N. Koirala, J. Moon, S. Oh, and N. P. Armitage, Quantized Faraday and Kerr rotation and axion electrodynamics of a 3D topological insulator, Science **354**, 1124 (2016).

[56] N. Tesařová, T. Ostatnický, V. Novák, K. Olejnik, J. Šubrt, H. Reichlová, C. T. Ellis, A. Mukherjee, J. Lee, G. M. Sipahi, J. Sinova, J. Hamrle, T. Jungwirth, P. Němec, J. Černe, and K. Výborný, Systematic study of magnetic linear dichroism and birefringence in (Ga,Mn)As, Phys. Rev. B **89**, 085203 (2014).

[57] V. K. Sang-Wook Cheong, Diyar Talbayev, and A. Saxena, Broken symmetries, non-reciprocity, and multiferroicity, npj Quantum Mater. **3**, 19 (2018).

[58] Y. Lubashevsky, L. D. Pan, T. Kirzhner, G. Koren, and N. P. Armitage, Optical Birefringence and Dichroism of Cuprate Superconductors in the THz Regime, Phys. Rev. Lett. **112**, 147001 (2014).

[59] R. Nandkishore and L. Levitov, Polar Kerr Effect and Time Reversal Symmetry Breaking in Bilayer Graphene, Phys. Rev. Lett. **107**, 097402 (2011).

[60] W.-K. Tse and A. H. MacDonald, Giant Magneto-Optical Kerr Effect and Universal Faraday Effect in Thin-Film Topological Insulators, Phys. Rev. Lett. **105**, 057401 (2010).

[61] A. Singh, K. I. Bolotin, S. Ghosh, and A. Agarwal, Nonlinear optical conductivity of a generic two-band system with application to doped and gapped graphene, Phys. Rev. B **95**, 155421 (2017).

[62] A. Singh, S. Ghosh, and A. Agarwal, Nonlinear and anisotropic polarization rotation in two-dimensional Dirac materials, Phys. Rev. B **97**, 205420 (2018).

[63] A. A. Zyuzin and R. P. Tiwari, Intrinsic anomalous Hall effect in type-II Weyl semimetals, JETP Lett. **103**, 717 (2016).

[64] S. P. Mukherjee and J. P. Carbotte, Absorption of circular polarized light in tilted type-I and type-II Weyl semimetals, Phys. Rev. B **96**, 085114 (2017).

[65] S. P. Mukherjee and J. P. Carbotte, Imaginary part of Hall conductivity in a tilted doped Weyl semimetal with both broken time-reversal and inversion symmetry, Phys. Rev. B **97**, 035144 (2018).

[66] S. P. Mukherjee and J. P. Carbotte, Doping and tilting on optics in noncentrosymmetric multi-Weyl semimetals, Phys. Rev. B **97**, 045150 (2018).

[67] T. Yoshino, Theory for oblique-incidence magneto-optical Faraday and Kerr effects in interfaced monolayer graphene and their characteristic features, J. Opt. Soc. Am. B **30**, 1085 (2013).

[68] N. Tesarova, P. Nemec, E. Rozkotova, J. Subrt, H. Reichlova, D. Butkovicova, F. Trojanek, P. Maly, V. Novak, and T. Jungwirth, Direct Measurement of the Three-Dimensional Magnetization Vector Trajectory in GaMnAs by a Magneto-Optical Pump-and-Probe Method, Appl. Phys. Lett. **100**, 102403 (2012).

[69] J. P. Carbotte, Dirac cone tilt on interband optical background of type-I and type-II Weyl semimetals, Phys. Rev. B **94**, 165111 (2016).

[70] A. K. Gabor Szechenyi, Mate Vigh, and J. Cserti, Transfer matrix approach for the Kerr and Faraday rotation in layered nanostructures, J. Phys.: Condens. Matter **28**, 375802 (2016).

[71] X.-L. Qi, T. L. Hughes, and S.-C. Zhang, Topological field theory of time-reversal invariant insulators, Phys. Rev. B **78**, 195424 (2008).

[72] S. Visnovsky, *Optics in Magnetic Multilayers and Nanostructures*, Optical Science and Engineering (CRC Press, 2006).

[73] J. Shibata, A. Takeuchi, H. Kohno, and G. Tatara, Theory of electromagnetic wave propagation in ferromagnetic Rashba conductor, J. Appl. Phys. **123**, 063902 (2018).

[74] A. J. Frenzel, C. C. Homes, Q. D. Gibson, Y. M. Shao, K. W. Post, A. Charnukha, R. J. Cava, and D. N. Basov, Anisotropic electrodynamics of type-II Weyl semimetal candidate WTe_2, Phys. Rev. B **95**, 245140 (2017).